

Fabrication of Visible Light Active Mn-Doped Bi₂WO₆-GO/MoS₂ Heterostructure for Enhanced Photocatalytic Degradation of Methylene Blue

Noor Tahir

University of Agriculture

Muhammad Zahid (✉ rmzahid@uaf.edu.pk)

University of Agriculture <https://orcid.org/0000-0001-8407-6886>

Ijaz Ahmad Bhatti

University of Agriculture

Yasir Jamil

University of Agriculture

Research Article

Keywords: Heterogenous Photocatalysis, Wastewater treatment, Semiconductor metal oxides, nanocomposites, doping, graphene Oxide.

Posted Date: May 13th, 2021

DOI: <https://doi.org/10.21203/rs.3.rs-438176/v1>

License:   This work is licensed under a Creative Commons Attribution 4.0 International License.

[Read Full License](#)

Version of Record: A version of this preprint was published at Environmental Science and Pollution Research on August 28th, 2021. See the published version at <https://doi.org/10.1007/s11356-021-16094-5>.

1 **Fabrication of visible light active Mn-doped Bi₂WO₆-GO/MoS₂ heterostructure for**
2 **enhanced photocatalytic degradation of methylene blue**

3

4 Noor Tahir ^a, Muhammad Zahid ^{a,*}, Ijaz Ahmad Bhatti ^a, Yasir Jamil ^b

5 ^a Department of Chemistry, University of Agriculture, Faisalabad- 38040 Pakistan

6 ^b Department of Physics, University of Agriculture, Faisalabad- 38040 Pakistan

7 *Corresponding Author Email: Zahid595@gmail.com; rmzahid@uaf.edu.pk

8 **Abstract**

9 The increase in environmental pollution has led to an increased investigation in the development of
10 novel ternary photocatalytic systems for remediation. These Photocatalytic systems exhibit superior
11 photocatalytic action for the removal of pollutants because of their visible light active bandgaps. A
12 highly effective visible light active ternary heterojunction was fabricated using a hydrothermal method
13 assisted by ultrasonication. Herein, we report the Insitu hydrothermal synthesis of Mn-doped Bi₂WO₆-
14 GO/ MoS₂ photocatalyst, efficiently exhibiting greater photocatalytic activity for the wastewater
15 treatment under solar light. The binary metal sulphide (MoS₂) used as a co-catalyst, acted as electron
16 collector and Graphene oxide (GO) as a support material for interfacial electron transfer to and from
17 bismuth tungstate and MoS₂. The as-prepared samples were characterized using SEM-EDX, FT-IR,
18 XRD, XPS, and UV–Vis techniques. The bandgap of the novel photocatalyst was found in the visible
19 region (2.2 eV) which helped in suppressing photoinduced electron-hole pairs recombination. The
20 ternary Mn-BMG showed 99% methylene blue removal after 60 minutes of sunlight irradiation at the
21 optimum conditions of pH 8, catalyst dose 50 mg/100ml and initial MB concentration of 10ppm under
22 sunlight irradiation. The Mn-BMG has proved to be an effective sunlight active photocatalyst that can
23 be reused without substantial loss in photocatalytic efficiency.

24

25 **Keywords:** Heterogenous Photocatalysis; Wastewater treatment; Semiconductor metal oxides;
26 nanocomposites; doping; graphene Oxide.

27

28 **1. Introduction:**

29 Water pollution and energy crisis has become a global threat due to rapid industrialization. Various
30 industries like textile, pharmaceutical, paper, cosmetics and food industry utilize organic dyes for
31 refining the quality of their manufactured products. These industries frequently produce an extensive
32 load of untreated dye wastewater, making dyes a major component of water pollution (Aziz et al., 2020).
33 Methylene Blue (MB) dye is an immensely used coloring agent for coloring silk, cotton and wood
34 products. Owing to the complex aromatic structure, the dye methylene blue is resistant to oxidation and
35 degradation by conventionally available methods. Exposure and utilization of water having traces of
36 this dye may cause serious health hazards in humans and animals including nausea, difficult breathing,
37 cyanosis, jaundice, and irritation on the skin and in the eyes. Hence, an appropriate method for the
38 removal of such poisonous dyes is crucial in present times of water shortage (Nawaz et al., 2020).
39 Advanced oxidation processes have received considerable importance because of their role in
40 wastewater treatment and water disinfection. Among Advanced oxidation processes, photocatalysis is
41 considered a green technology because of the utilization of solar energy at ambient conditions (Mushtaq
42 et al., 2020). Heterogeneous Photocatalysis is now a promising strategy to address the wastewater crisis
43 owing to the generation of light-induced electrons and holes which can easily scavenge H₂O molecules
44 O₂ and produce reactive oxygen species. Hence, Using solar energy one can convert recalcitrant organic
45 pollutants into harmless compounds (Mudhoo et al., 2020). Ternary metal tungstates have been used
46 for water purification owing to their narrow bandgaps, low-cost applicability, crystallinity and effective
47 utilization of sunlight because of their narrowband gaps (Singh et al., 2020). These ternary compounds
48 suffer from the limitation of high charge carrier's recombination. The photocatalytic efficiency of the
49 ternary metal oxides irradiation can be enhanced by coupling with other semiconductor materials having
50 a narrow bandgap and support materials or via doping with transition or plasmonic metals under sunlight
51 (Saher et al., 2021). Since the formation of heterojunctions via coupling and doping both can be
52 effective for suppression of e⁻/h⁺ recombination by providing new pathways to charge carriers (Mafa
53 et al., 2019). Bismuth tungsten oxide (Bi₂WO₆), is an important member of ternary Aurivillius metal
54 oxides having perovskite layered crystal structure. The sandwich structure consists of alternating layers
55 of (Bi₂O₂)²⁺ and octahedral WO₄²⁻. This interlayer spacing offers a large surface area and adequate active
56 sites for an efficient photocatalytic process and also prevents electrons and holes from recombining.
57 Bi₂WO₆ (BWO) has a narrow bandgap of (2.80 eV) which makes it efficient as a visible light active
58 photocatalyst as compared to binary compounds (Wang et al., 2017). Although BWO exhibits excellent
59 photodegradation efficiency towards organic pollutants, its activity is still hindered by some factors
60 including narrow photo-response limiting maximum utilization of solar light and high recombination
61 rate of charge carriers. Among various approaches being proposed in previous researches, the
62 construction of ternary novel heterojunctions via coupling and doping has widely been used to enhance
63 the charge separation efficiency (Li et al., 2018). Hence, the key step for the formation of novel ternary

64 heterojunctions is the selection of a suitable material for coupling with BWO ensuring maximum visible
65 light utilization. Among all methods to increase the visible light response of ternary compounds, doping
66 is a relatively effective method. These ternary hybrid photocatalytic systems can separate electrons and
67 holes more efficiently than binary nanocomposites. Doping alters the bandgap and atomic structure of
68 host material by the introduction of foreign ions. The introduction of additional energy levels helps in
69 trapping and separating electrons for a longer period of time hence preventing recombination. Transition
70 metal doping includes use of transition metals like Cobalt, niobium, manganese, zinc, tungsten, iron
71 and molybdenum for modifying the d-orbital configuration, the fermi level and the bandgap (Huang et
72 al., 2016). The transition metals have partially filled d orbitals which helps in the formation of new
73 energy bands below the conduction band of host material. These newly formed energy bands are
74 responsible for redshift in the bandgap energy enabling photocatalysts to act efficiently in the visible
75 range of light spectra (Ahmad, 2019).

76 Molybdenum disulfide (MoS_2) is a typical layered two-dimensional layered binary compound
77 particularly used as a hybrid co-catalyst material. A large number of nanocomposites coupled with
78 MoS_2 have been reported which showed enhanced activity because of the existence of S-atoms on
79 exposed ends of MoS_2 (Lv et al., 2017). But, the overall photocatalytic reaction activity of MoS_2 alone
80 is reduced due to poor electrical conductivity. Besides the effectiveness of Bi_2WO_6 as a visible light
81 active catalyst and its coupling with MoS_2 , a suitable mediator is required for transferring electrons
82 efficiently.

83 The presence of Graphene oxide provides enhanced surface area because of the two-dimensional
84 assembly of carbon atoms which are all Sp^2 hybridized and covalently linked. The electrically
85 conductive large surface area of graphene oxide helps in effective charge migration and acts as a
86 mediator for shuttling electrons between available active sites of photocatalyst and co-catalysts,
87 subsequently suppressing the electrons and holes from reuniting, accelerating the overall catalytic
88 process (Tabasum et al., 2020). Also, Graphene oxide adsorbs organic pollutants well on the surface
89 of photocatalysts besides enhancing their photo-response. Hence, the graphene supported ternary
90 heterojunctions greatly improve the overall activity of ternary nanocomposites under visible light
91 irradiation.

92 Herein, we report the synthesis of Mn-doped Bi_2WO_6 -supported over Graphene oxide and coupled with
93 binary metal sulphide MoS_2 by adjusting the weight percentage of each component in the ternary
94 composite. A simple in situ hydrothermal synthesis process was employed for the fabrication of novel
95 Mn-BMG and was employed for the cationic dye Methylene blue (MB) degradation under sunlight.
96 Meanwhile, the characterization studies of the prepared catalysts were done by techniques like FTIR,
97 SEM-EDX, XPS, XRD and UV-Vis spectroscopy. The studies showed that Graphene oxide supported
98 Mn- Bi_2WO_6 coupled with MoS_2 provided enhanced surface area and an easy pathway for the transport
99 and separation of photogenerated charge carriers effectively increasing the visible light response of
100 photocatalyst.

101

102 **2. Experimental and synthesis**

103 **2.1. Materials and Reagents:**

104 Sodium tungstate dihydrate ($\text{Na}_2\text{WO}_4 \cdot 2\text{H}_2\text{O}$), Sodium molybdate dihydrate ($\text{Na}_2\text{MoO}_4 \cdot 2\text{H}_2\text{O}$), Bismuth
105 nitrate pentahydrate $\text{Bi}(\text{NO}_3)_3 \cdot 5\text{H}_2\text{O}$, Sodium Nitrate (NaNO_3), Potassium permanganate (KMnO_4),
106 Ethylene glycol (analytical grade), Sulphuric acid (H_2SO_4) and Hydrogen peroxide were obtained from
107 (Sigma Aldrich), Manganese chloride $\text{MnCl}_2 \cdot 4\text{H}_2\text{O}$ were obtained from UNI-Chem reagents. Graphite
108 Powder and thioacetamide $\text{C}_2\text{H}_5\text{NS}$ were obtained from Sharlau. Dye methylene blue was purchased
109 from Fischer scientific company. All chemicals used were of analytical grade and used without any
110 further purification. Distilled water was used for all the reaction solutions throughout the study.

111

112 **2.2. Synthesis of Graphene Oxide:**

113 Graphene oxide (GO) was synthesized by a modified hummers method. as previously reported in our
114 work (Tabasum et al., 2019). The detailed information is present in the supplementary material.

115

116 **2.3. Synthesis of Mn-BWO-GO/MoS₂ (Mn-BMG)**

117 Initially, $\text{Bi}(\text{NO}_3)_3 \cdot 5\text{H}_2\text{O}$ (5mmol) was dissolved in 30ml Ethylene glycol (Solution A) and
118 $\text{Na}_2\text{WO}_4 \cdot 2\text{H}_2\text{O}$ (2.5mmol) was dissolved in 30ml distilled water termed Solution B. The prepared
119 solution B was added dropwise in solution A under vigorous stirring. Mn doping (10 mol%) was done
120 by adding precursor $\text{MnCl}_2 \cdot 4\text{H}_2\text{O}$ (0.0178gm) directly in the above solution and the whole mixture was
121 magnetically stirred for two hours and poured in a Teflon lined stainless steel autoclave for
122 hydrothermal treatment for 24 hours at 180°C temperature. A white powder was obtained after
123 centrifugation and washing thrice with distilled water and ethanol was oven-dried at 60°C. Next, an in-
124 situ hydrothermal method was performed in which 2.5mmol of Sodium molybdate and 5mmol of
125 thioacetamide was dissolved in 30ml distilled water to form MoS_2 (Solution C). The whole mixture was
126 stirred magnetically for two hours. The above prepared Mn-BWO in 50wt% was dissolved with
127 magnetic stirring in 20 ml distilled water and added dropwise to solution C. Meanwhile, Graphene oxide
128 20wt% (0.2gm), prepared above was ultrasonically dispersed in 20ml distilled water for about 30
129 minutes and added dropwise to Solution C. The whole mixture was vigorously stirred for another three
130 hours until a homogenous solution was obtained. The whole mixture was again given hydrothermal
131 treatment at 180°C for 24 hours by pouring the reaction mixture in a 250ml capacity autoclave. The
132 prepared black powder was centrifuged, washed thrice using distilled water and ethanol and dried in an
133 electric oven at 60°C for 12 hours. The ternary BWO-GO/ MoS_2 (BMG) was prepared by a similar
134 method except for the addition of $\text{MnCl}_2 \cdot 4\text{H}_2\text{O}$. The binary BW-GO (BG) was prepared by a method
135 reported earlier by Nguyen and his fellows (Nguyen et al., 2018).

136 **2.4. Characterization and equipment.**

137 The microstructure, morphology and elemental analysis of as prepared ternary Mn-BMG and BMG
138 were characterized using a Scanning electron microscope equipped with EDX (SEM-EDX; FEI NOVA
139 450 NANOSEM). The crystalline properties of all powder samples were measured by XRD (Bruker D8
140 Advanced equipment operated) over a range of 2θ values from 5-85 degrees. The presence of several
141 functional groups on the surface of prepared photocatalysts was studied by Fourier transform infrared
142 spectroscopy (FTIR, Thermo Nicolet). The XPS analysis was done to study the elemental states and the
143 surface chemical compositions investigated (Escalab 250 XPS system, Thermo Fisher Scientific UK).
144 The bandgap analysis of the ternary doped and undoped samples was done using UV–VIS
145 spectrophotometer (Cecil CE 7200) in the 200-800 nm range by dispersing catalysts in water under
146 ultrasonication.

147 **2.5. Evaluation of photocatalytic degradation**

148 Various experiments on the photocatalytic degradation of cationic dye methylene blue (MB) were
149 carried out under sunlight in batch mode using ternary Mn-BMG, BMG and binary BG nanocomposites
150 for one hour. The nanocomposites in different concentrations were initially screened in Ultraviolet and
151 Visible irradiation to check the feasibility of the MB degradation. The effect of several parameters
152 including pH (2–9), catalyst dosage (10–100mg/100ml), initial dye concentration (2–20 ppm) and
153 irradiation time (10–120 min) on MB photodegradation was studied. For comparison, a single
154 experiment was performed under UV irradiation for each catalyst at their optimum conditions. The
155 control experiments of Dye/Sunlight, Dye/UV, Dye/UV light/catalyst were also run to examine the dye
156 removal under these conditions also. For the photocatalytic degradation of MB under sunlight, the
157 desired quantities of catalysts were dispersed via ultrasonication in 100 mL of 10 ppm dye solution.
158 Before exposing the solutions to sunlight, the solutions were stirred mechanically in dark to obtain
159 adsorption-desorption equilibrium for nearly thirty minutes. Before exposure to any light source, the
160 adsorption capacity of samples was examined. After checking the adsorption capacity of photocatalysts,
161 the dye solutions were kept under sunlight irradiation for about 60 min at 180 rpm in electrical orbital
162 shakers. After each trial, the nanocomposites were separated from the solution by centrifugation of 5ml
163 dye solution and the concentration of the remaining dye was determined by taking absorbance of clear
164 solution using a UV–VIS spectrophotometer at 665nm. A blank beaker of dye solution was also kept in
165 dark and sunlight to investigate dye degradation in the presence and absence of light. The % degradation
166 was calculated using the following formula

$$167 \quad \% \text{ Degradation} = 1 - \frac{A}{A_0} \times 100 \quad \text{Eq. (1)}$$

168 Here, A_0 is the initial absorbance and A is absorbance after treatment under solar light. The pH was
169 maintained by using different molar concentration solutions of HCl and NaOH using a pH meter (Ohaus
170 ST3100, USA). The sunlight intensity was measured by a solar power meter (SM206), and the

171 brightness was measured by a light meter (HS1010A). The reusability of catalysts was investigated by
172 5 times recycling the catalysts and reusing at optimum conditions under sunlight each time with freshly
173 prepared 10 ppm MB solution.

174

175 **3. Characterization**

176 **3.1. FTIR Analysis:**

177 FTIR analysis was employed to elucidate the existence of several functional groups and chemical bond
178 formation in the doped and undoped ternary BMG samples as shown in figure 3.1. Transmittance peaks
179 were observed around 645, 948 1024, 1069, 1380, 1450 and 1620 cm^{-1} for the ternary nanocomposites.
180 The peaks at around 1024 cm^{-1} and 1069 cm^{-1} have appeared because of O=S=O asymmetric stretching
181 vibrations and S-O-S symmetric vibrations, respectively. Additionally, the presence of a peak at 1185
182 cm^{-1} shows asymmetric vibrations of Mo-O bonds confirming the synthesis of MoS₂ as described in
183 previous studies (Zolgharnein et al., 2018). An elongated broad band from 645 cm^{-1} and 845 cm^{-1} is
184 accredited to Bi-O and W-O stretching vibrations. A peak at 715.46 cm^{-1} explains the antisymmetric
185 bridging mode which is associated with tungstate chains. An intense peak present at 1384 cm^{-1} explains
186 the bending vibrations of W-O-W. These characteristic bands of BW were observed for all samples.
187 (Khojeh et al., 2017). The absorption band appearing at 1450 cm^{-1} , 1557.9 cm^{-1} , and 1630.75 cm^{-1}
188 indicates the formation of COO⁻, C=C and C=O stretching vibrations indicating successful fabrication
189 of GO and incorporation of GO into BW (Hu et al., 2019). The skeletal vibrations of graphene sheets
190 appearing at 1630.75 cm^{-1} indicate carbonyl stretching that the oxygen-comprising groups in GO are
191 decomposed upon exposure to a hydrothermal environment. But no other obvious absorption peak
192 related to GO could be observed in the composites due to the low content of GO (Liu et al., 2017).
193 These vibrations appearing at 1630 cm^{-1} may also indicate adsorbed water molecules and unoxidized
194 graphitic domains (Hou et al., 2020) A very small peak is visible at 947 cm^{-1} in Mn-doped ternary
195 composite as compared to undoped ternary sample, which is ascribed to Mn-O vibrations as confirmed
196 from previous studies (Ahmad et al., 2019). Besides, the peak intensity is reduced in the doped ternary
197 composite, which supports the successful insertion of dopant ions into the host material.

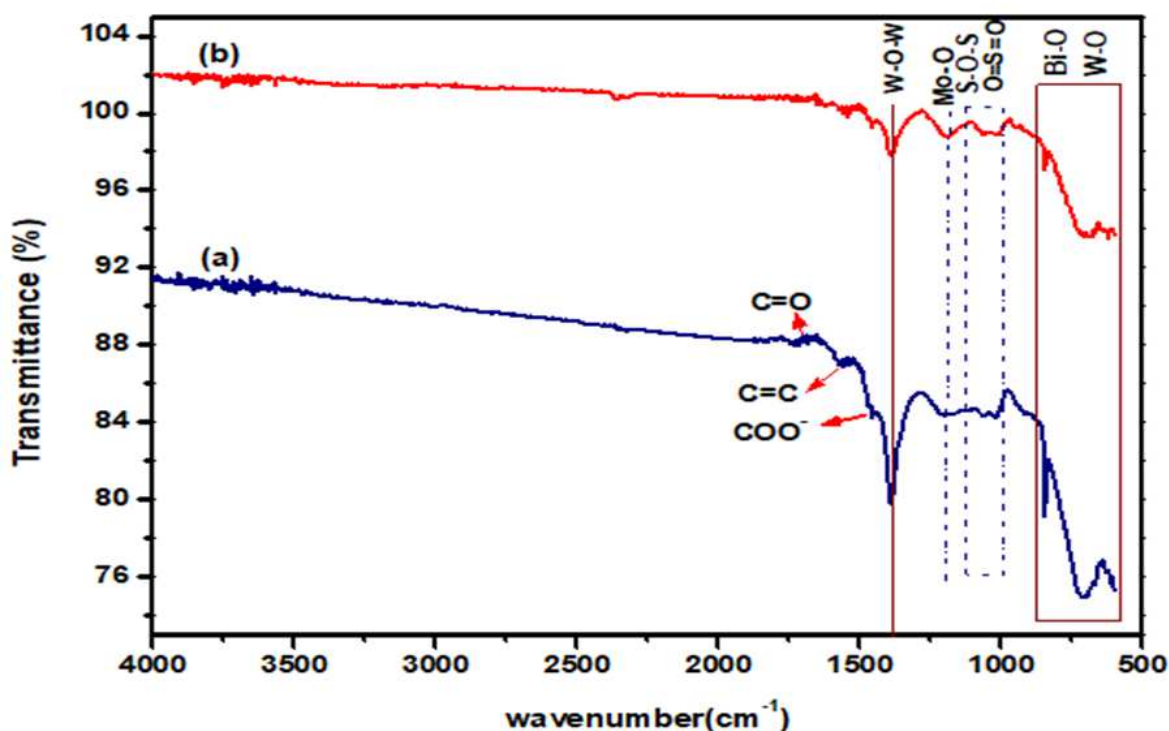


Fig. 1. FTIR spectra of (a) BMG and (b) Mn-BMG ternary nanocomposites

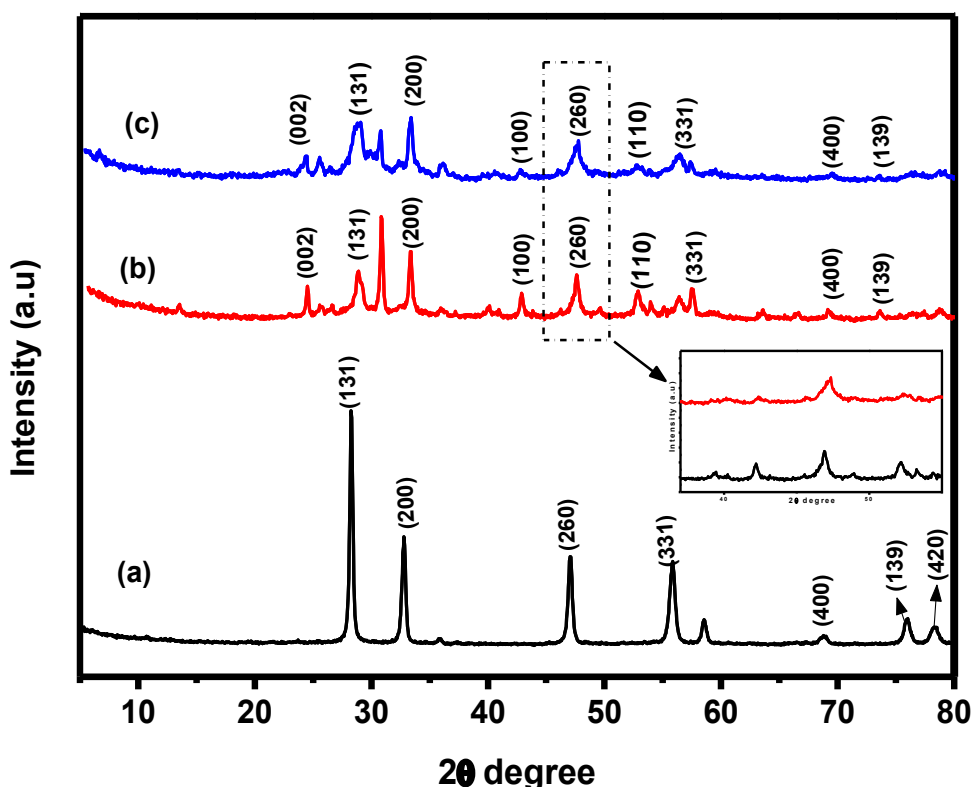
3.2 XRD analysis:

The phase purity and crystalline structures of all the ternary and binary samples were studied by XRD characterization in 2θ range of $5-85^\circ$ as shown in Figure 3.2. The influence of manganese doping and GO/MoS₂ coupling on the crystalline structure of bismuth tungstate were also affirmed through XRD. All the strong diffraction peaks of Bi₂WO₆ are readily indexed at 2θ values 28.02° , 32.8° , 47.12° and 55.7° , well assigned to (131), (200), (260) and (331) crystal planes indicating the successful formation of Bi₂WO₆ in orthorhombic phase. The sharp diffraction peaks of bismuth tungstate in all samples including Mn-BMG, BMG, and BG are the same showing formation of high purity and crystalline single-phase orthorhombic bismuth tungstate, showing that the addition of MoS₂ And GO has not affected the orthorhombic structure of bismuth tungstate. The peaks at 2θ values of 39.2° and 52.2° corresponding to (100) and (110) planes, indicating the formation of amorphous molybdenum disulphide. No other visible peaks of MoS₂ are observed suggesting low crystallinity and trace loading of MoS₂ on the GO support. The reported peak of Graphene oxide at 10° disappears and appears at 23.5° indexed (002), exhibiting that the Graphene oxide is a highly oxidized product. No extra visible peaks of graphene oxide could be detected in all the XRD patterns owing to the less content and stacking of GO in the ternary nanocomposite, (Zhou et al., 2019). The fewer XRD patterns of GO in ternary hybrids shows stacking of GO and its function as a substrate for nucleation and growth of MoS₂ upon exposure to hydrothermal treatment (Li et al., 2015) The absence of any impurity peak in the Mn-BMG sample infers the effective substitution of divalent cations (Mn²⁺) in the bismuth tungstate matrix. The peaks in the XRD pattern of Mn-doped samples are lower in intensity as compared to the undoped ternary

220 composite sample. Additionally, a peak shift to higher diffraction angles position has also been observed
 221 in the Mn-doped sample as compared to the undoped sample suggesting that the Mn^{2+} ions successfully
 222 doped the host ternary composite. This peak shift suggests changes in interstitial Bi_2WO_6 unit cell
 223 volume as a result of doping. The ionic radius of Bi^{+2} ions is larger than that of Mn^{2+} ions, hence Mn^{2+}
 224 ions can enter Bi_2WO_6 host lattice and substitute Bi^{+2} ions, causing the XRD pattern to shift to higher
 225 diffraction angles (inset of fig.3.2.) Similar outcomes of Mn doping in host lattice were also observed
 226 by Reddy et al (Reddy et al., 2019). The average particle size was calculated using Debye-Scherrer
 227 formulae equation 3:

$$D = 0.9\lambda/\beta\cos\theta \quad \text{Eq..... (2)}$$

228
 229 D is the particle size, λ is the wavelength of $CuK\alpha$ (i.e., 0.154 nm), β explains the intensity at full-width
 230 half maximum of diffraction line which is expressed in radians and θ refers to Bragg's angle. The
 231 average particle size of undoped and doped particles was found to be 24.2nm and 20.1nm respectively.
 232 The smaller crystallite size of Mn-doped nanocomposite can be referred to as the better growth of
 233 nanoparticles onto support media but having restricted dimensions which may distort host lattice due to
 234 insertion of Mn^{+2} ions decreasing nucleation and grain growth (Chanu et al., 2019).

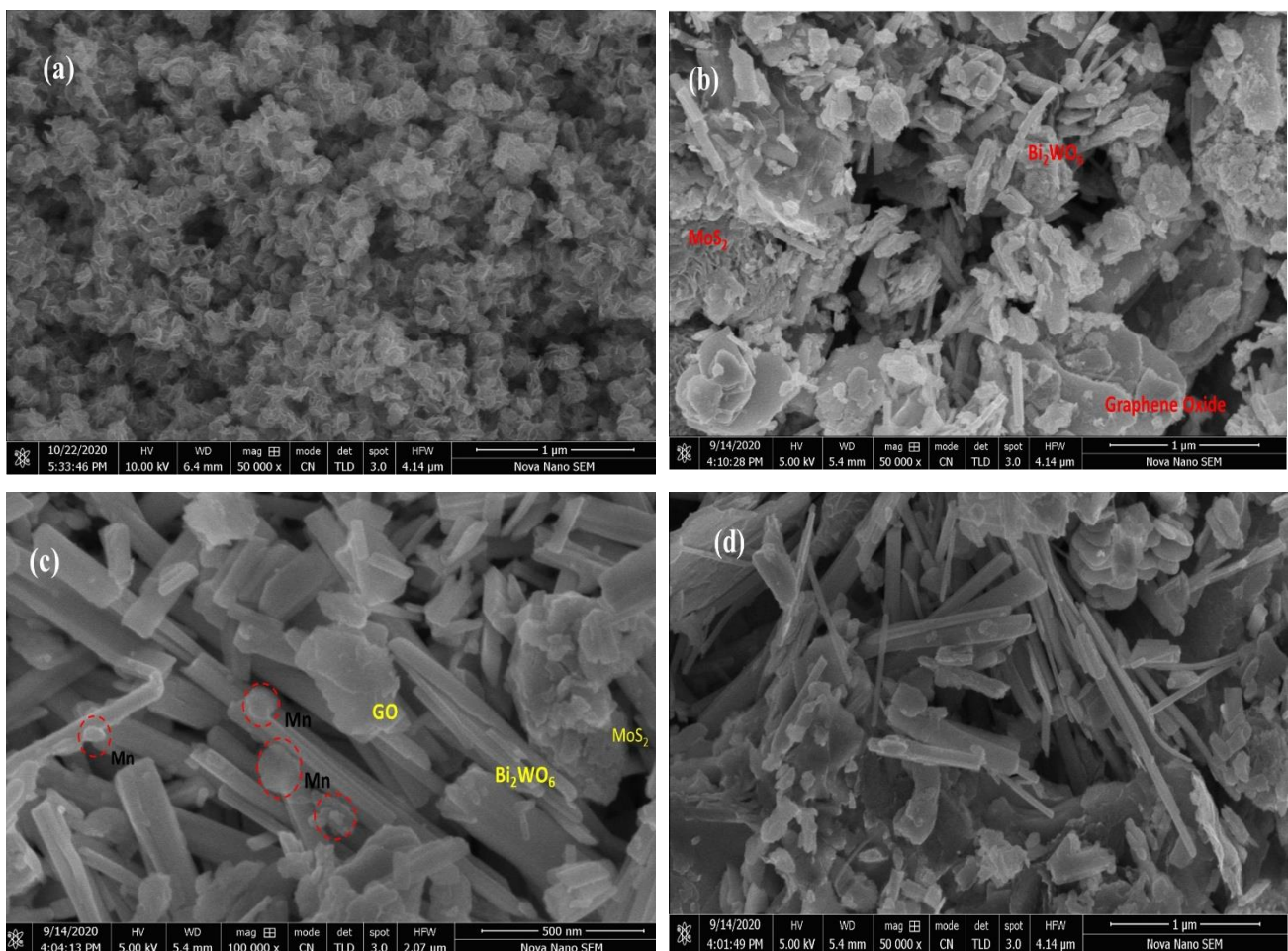


235
 236 **Fig.2** X-ray diffraction patterns of (a) BG (b) BMG and (c) Mn-BMG nanocomposites

237 **3.3 SEM analysis:**

238 The morphology and microstructure of as-synthesized pristine and doped samples were investigated by
 239 Scanning electron microscope (SEM) at various resolutions. SEM images determined the
 240 morphological changes after doping in the surface of the ternary nanocomposite. After combining Mn-
 241 BWO with MoS₂ and GO the ternary hybrid showed a hierarchical structure showing the assembly of
 242 plenty of bismuth tungstate nanorods interlaced and flower-like nanostructured MoS₂ distributed over
 243 stacked graphene sheets fig 3(c). The MoS₂ exhibited nanoflowers-like morphology as in fig 3.3 (a) and
 244 are clearly shown growing on the edges alongside stacking of graphene oxide ternary heterostructure
 245 of SEM images fig (3.3b). The undoped ternary composite exhibited severe agglomeration due to the
 246 stacking of graphene oxide. The exterior coarse texture of BW nanoplates is because of coverage and
 247 stacking of GO sheets However, this agglomeration notably weekend after the introduction of Mn in
 248 the nanocomposite. This suggests that Mn doping effectively suppressed the severe aggregation of
 249 particles (Dou et al., 2020). The Mn-doped BWO-graphene shows uniformed surface nanorods and less
 250 agglomeration. The ternary doped nanocomposite with all the components present, well separated with
 251 minimized aggregation, uniform structure and Mn particles uniformly attached to BW rods fig 3.3 (c
 252 &d). Hence, the incorporation of Mn in the host lattice influenced the morphology of the particles.

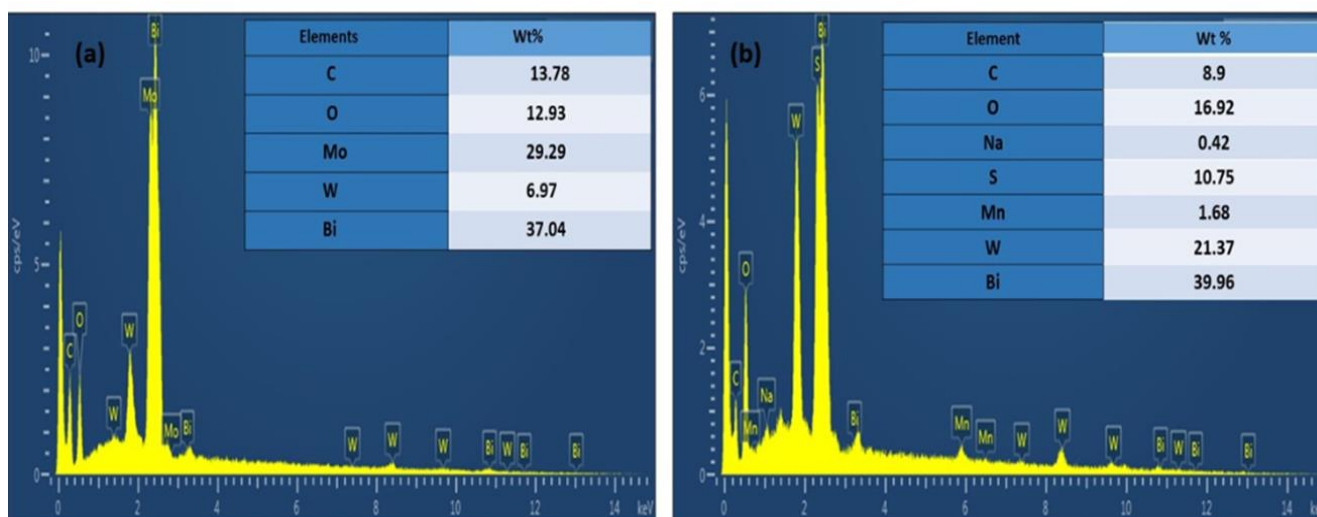
253
 254



255 **Fig.3** SEM images of (a) MoS₂ nanoflowers (b) BMG (c &d) Mn-BMG

256 3.4 EDX analysis:

257 EDX elemental mapping confirmed the chemical configuration and distribution of Bi, W, C, S, N, O
258 according to their nominal weight percentages as shown in fig 3.4. The undoped ternary BWO-GO/MS
259 did not show the presence of any impurity atom whereas the EDX pattern of doped ternary hybrid shows
260 Mn atom in 1.68 Wt% which is also confirmed by the XPS spectra, suggesting successful incorporation
261 of Mn in ternary nanocomposite according to their nominal chemical stoichiometry amounts. It also
262 confirms the presence of all other elements including Bi, W, O, C, Mo, S and Na. Little changes in the
263 wt% of all elements is observed after the hydrothermal processing.
264

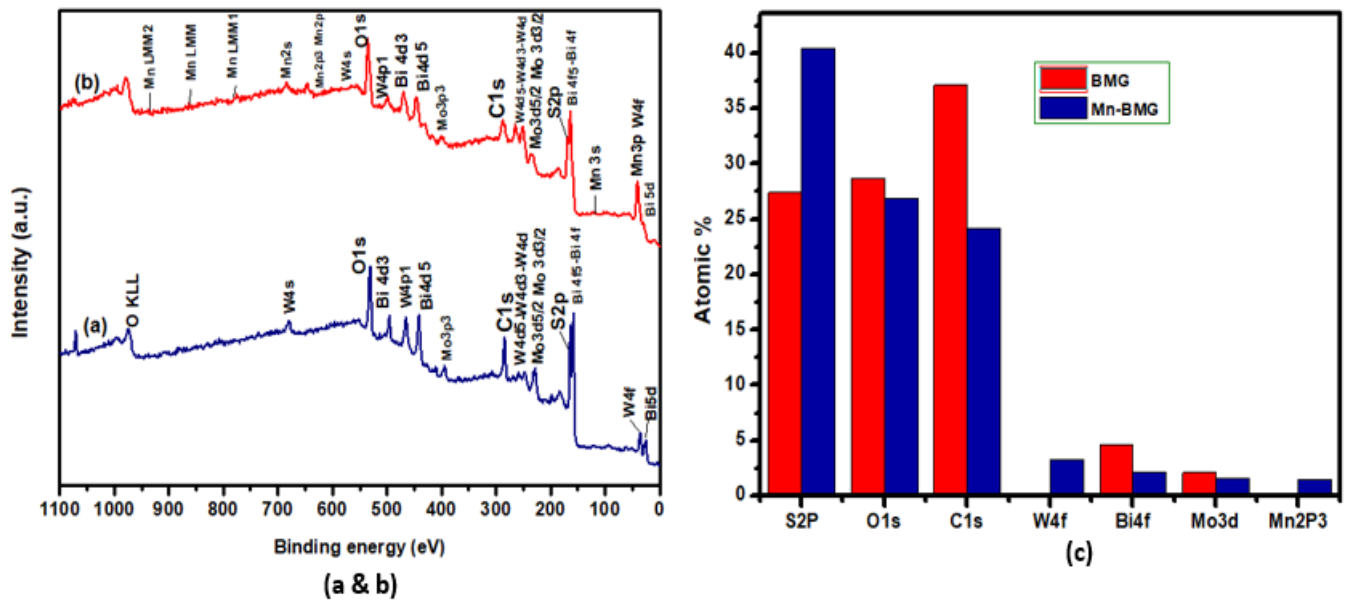


265

266 **Fig.4** EDX spectra of (a)BMG (b) Mn- BMG ternary nanocomposites

267 3.5 XPS analysis:

268 The composition and chemical states of all the elements present and the interactions among all the three
269 components in the ternary nanocomposite is analyzed by XPS spectra. The elemental composition of
270 BMG and Mn-BMG was investigated through XPS survey scan which revealed the peaks of Bi
271 (165.06eV), W(37.81eV), O1s (534.82eV), S (163 eV), C (284.17eV) and Mn as shown in fig (3.5a)
272 while the atomic percentage of detected elements were shown in fig (3.5b). The Bi 4f peak appearing
273 at a binding energy of 165.067eV ascribed to Bi 4f₇ and Bi 4f₅ Bi⁺³ ions in Bi₂WO₆ nanoparticles. The
274 O1s peak in the ternary component at a binding energy of 536.0eV is assigned to the metal-oxygen
275 bonds of Bi₂WO₆ and also to the adsorbed water molecules on the catalyst's surface.
276 The C1s peak at 283.74eV is possibly credited to the adventitious residual carbon as also confirmed
277 from previous studies (Yang et al., 2015). A peak earing at a binding energy of 1011eV is assigned to
278 Mn²⁺, respectively, indicating the presence of Mn²⁺. Characteristic peaks appearing at 648.04eV and



279 684.27eV are ascribed to Mn2p_{3/2}, Mn2p_{1/2}, Mn2s respectively. Thus XPS data confirms the presence
 280 of Mn ions in doped ternary nanocomposite (Dou et al., 2020). The XPS of Wf₄ can be detected at
 281 37.81eV suggesting W 4f_{5/2} of W₆₊. The peak at 163 eV is the S2p peak matched exactly well with the
 282 S²⁻ binding energy which is required for MoS₂ formation. Also, the peaks at 229.60 confirm the
 283 presence of Mo 3d_{5/2} and Mo 3d_{3/2}, indicating the dominant presence of Mo⁴⁺ species (Senthil et al.,
 284 2019). The atomic percentage of S2p, O1s, C1s, W4f, Bi4f, Mo3d, Mn2p₃ is 40.4%, 26.9%, 24.2%,
 285 3.3%, 2.1%, 1.6%, 1.5% respectively in Mn-BMG, while the undoped counterpart comprised of C1s,
 286 O1s, S2p, Bi4f, Mo3d, W4f in 37.1%, 28.7%, 27.4%, 4.6%, 2.1%, 0.2% atomic percentages
 287 respectively.

288

289

290 **Fig.5** XPS survey spectrum of (a) BMG (b) Mn-BMG and (c) atomic percentages of BMG and Mn-
 291 BMG

292

293 3.6 Optical Analysis

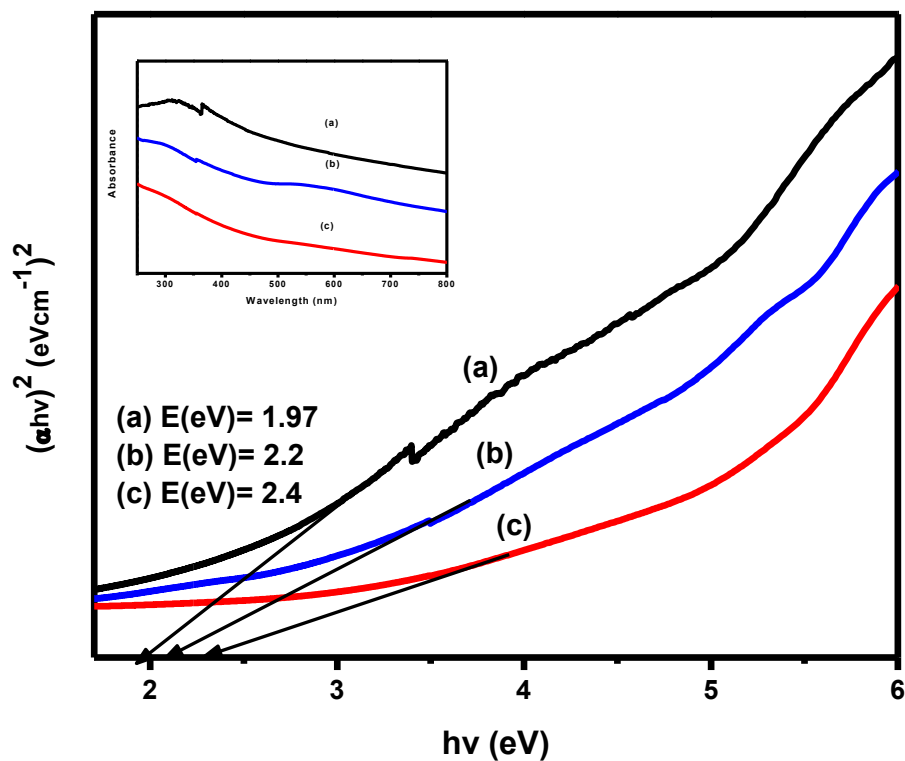
294 The optical response was measured by observing UV-VIS absorption spectra and determine the
 295 bandgap energies of pure and Mn-doped ternary nanocomposite in the range of 200-900nm. The
 296 absorption edge of the Mn-doped BWO-GO/MoS₂ nanocomposite was found in the visible region using
 297 the tauc plot. The Mn-doped BMG showed an even greater range of light absorption to the entire visible
 298 spectrum in comparison to the pristine ternary sample. The Mn doping in ternary heterojunctions
 299 improved the optical absorption providing a possibility to enhance photo-induced electron-hole pairs
 300 generation ultimately enhancing the photodegradation in the visible region. The bandgap energies of
 301 the catalysts were estimated using the formula given in equation 4.

302

303

$$(ahv)^2 = B(hv - E_g) \quad \text{Eq (3)}$$

304 Where $E_g = h\nu$ when $\alpha h\nu = 0$ and the $(\alpha h\nu)^2$ is plotted against energy in eV. The absorption energy
 305 taken at $h\nu$ value where it then extrapolates to $\alpha=0$ as shown in Fig. 5. The estimated band gap energies
 306 were found to be 2.4 eV and 2.2 eV for BMG and Mn-BMG. Here, α , B and ν are described as the
 307 absorption coefficient, proportionality constant and the light frequency. The optical studies show that
 308 all the photocatalysts show strong absorption in the visible light region.
 309



310
 311 **Fig.6** Bandgap energies estimation of (a) BG and (b) Mn-BMG (c) BMG by Tauc plot method with
 312 inset showing the UV-VIS absorption spectra of the BMG and Mn-BMG
 313

314 **4. Effect of Operational parameters:**

315 **4.1 Effect of pH:**

316 In the photodegradation process, the key factor that directly affects the photoefficiency of the
 317 photocatalytic system is the pH of the aqueous solution. The pH governs the surface charge
 318 characteristics of the photocatalysts according to their point of zero charges (pH_{PZC}) and also the
 319 adsorption capacity of the organic molecules on the surface of the catalyst (Ahmadi et al., 2020). The
 320 effect of pH on the photodegradation of MB was examined by changing pH values from 2 to 9 keeping
 321 all other factors constant (catalyst dose=50 mg/100mL for doped and undoped ternary and 40mg/100ml
 322 for binary BG, Initial dye concentration: 10ppm, and irradiation time 60 min). The pH of dye solutions
 323 was maintained using 0.1 M and 1mM solutions of sodium hydroxide hydrochloric acid. Methylene

324 blue is a cationic dye hence it is positively charged upon dissociation in water. The pH_{PZC} value for Mn-
325 BMG was determined at pH 6.2. At pH values lower than the pH_{PZC} , the surface of the catalyst is
326 positively charged and the positively charged MB dye molecules are electrostatically repulsed. In the
327 acidic medium, the active sites on the catalyst's surface are weak to produce hydroxyl radicals,
328 consequently decreasing the dye degradation (Nie et al., 2014). At pH values above 6.2, the catalyst's
329 surface is negatively charged and the cationic MB dye molecules were electrostatically attracted
330 towards the catalyst surface, enhancing the adsorptive property of dye molecules. The active sites on
331 the surface of the catalyst showed increased hydroxyl radicals production resulting in the increased MB
332 degradation in the basic medium. Hence, the ternary Mn-BMG showed 99% photocatalytic degradation
333 in an alkaline medium at optimum pH of 8 under visible light irradiation of 60 minutes as shown in fig.
334 7(a) The undoped ternary BMG at pH 8 and binary BG at pH 7 showed 95% and 92% degradation
335 respectively in the presence of sunlight for about the same time duration.

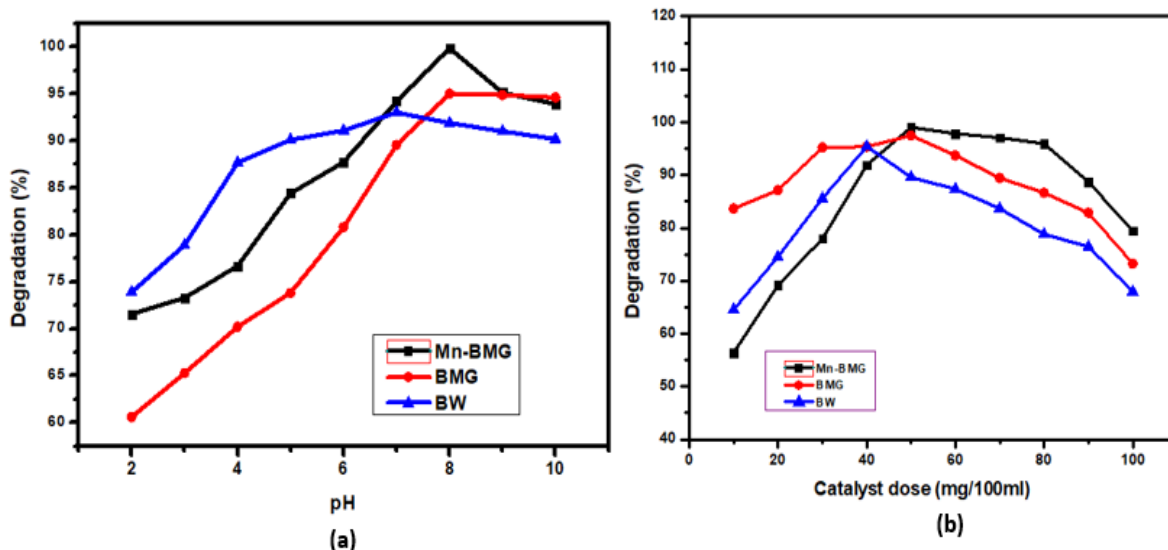
336 **4.2 Effect of catalyst dose:**

337 The amount of catalyst used is another important parameter for the evaluation of photocatalytic
338 performance and economic cost. To understand the relation among catalyst loading and
339 photodegradation efficiency, degradation of 10ppm MB dye solution was investigated in the range of
340 10-80mg/100mL, keeping all others factors constant (pH=8) for Mn-doped and undoped ternary, 7 for
341 binary BG, catalyst dose= optimum of each catalyst, and irradiation time 60 min. Photocatalyst dose
342 ranging from 10mg-100mg/L were used to study the influence on degradation. The photodegradation
343 efficiency of Mn-BMG enhanced from 69% to 99% as the catalyst dose was increased from 10mg to
344 50mg. The increase in catalyst dose enhances the number of active sites on the catalyst's surface,
345 consequently enhancing the production of hydroxyl and superoxide radicals. The undoped and doped
346 ternary composites showed enhanced photodegradation at an optimum catalyst dose of 50mg/ml and
347 binary BW-GO at 40mg/100ml as shown in graph b of fig 7(b). An increase in catalyst dose above 50
348 mg showed a slight increase up to 97% and started decreasing when it went beyond 100mg. This
349 reduction in degradation is owing to the interception of light preventing light photons to reach the
350 surface of adsorbed contaminant because of agglomeration of catalysts at their higher doses and
351 subsequent unavailability of active sites (Hu et al., 2019). Hence, catalyst dose decides the limits of a
352 catalyst for particular organic pollutants in wastewater above which the rate of degradation eventually
353 decreases. Graphene oxide-supported composites prevent agglomeration and show effective
354 degradation even at higher concentrations (Tabasum et al., 2021).

355 **4.3 Effect of initial dye concentration:**

356 The dye degradation is highly dependent upon the concentration of dye adsorbed on the catalyst surface.
357 The effect of initial dye concentrations ranging from 2-20ppm was studied for the photodegradation of
358 MB by Mn-BMG and all other nanocomposites keeping all other factors constant at their optimal values.
359 At initial low MB load, maximum degradation was attained which is linked to the availability of

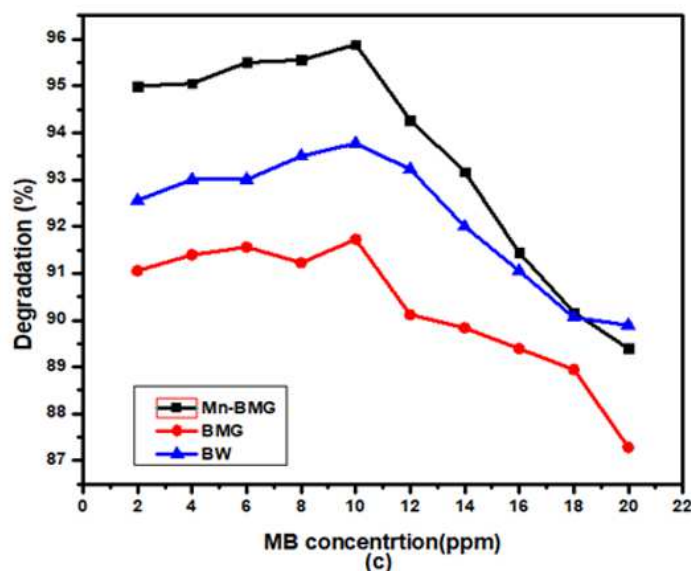
360 maximum active sites and also due to the reaction between dye molecules and hydroxyl radicals formed
361 on the catalyst's surface. As the dye concentration is increased, active sites on the catalyst surface
362 become saturated as more dye molecules are adsorbed on the surface. The number of photons reaching
363 the surface of the catalyst becomes fewer causing less generation of hydroxyl radicals for effective
364 degradation of MB molecules (Nawaz et al., 2020). The performance of all photocatalysts is shown in
365 graph c of fig 4.1. All catalysts showed maximum degradation at a methylene blue concentration of
366 10ppm. The ternary Mn-BMG nanocomposite showed above 90% degradation even at higher MB
367 concentrations. This is because the ternary heterojunction has enhanced surface area and can adsorb
368 enhanced concentration of MB molecules. The vacant active sites available after the degradation of
369 adsorbed dye molecules on the surface of the photocatalyst are rapidly occupied by other dye molecules
370 near the catalyst surface (Mushtaq et al., 2020). This results in enhanced MB degradation even at higher
371 dye loads by the novel Mn-BWO-GO/MoS₂ as compared to other photocatalysts
372



373
 374
 375
 376
 377
 378
 379
 380
 381

Fig. 7 Optimization of reaction parameters using Mn-BMG, BMG and BW (a) pH, (b) catalyst dose, (c) Initial dye concentration

4.4 Effect of irradiation time:



382 The maximum energy that is required for the initiation of photocatalytic reaction comes directly from
 383 the light energy hence, the conditions of light illumination have a great impact on the overall
 384 performance of photocatalysts. Fig shows the decomposition efficiency of MB over Mn-BMG, BMG
 385 and BG under sunlight irradiation. Under the optimum conditions for all catalysts, The dye solutions
 386 were exposed to light irradiation for various for about an hour. The UV-VIS absorption spectra of
 387 treated MB solutions after irradiation under sunlight were recorded in the 400-800nm range each after

388 ten minutes. The spectral changes in the treated dye solution were observed by plotting absorbance data
389 as a function of time. The trends show an increase in the degradation as time increases as shown in fig
390 S1(a, b, c for BMG, Mn-BMG, and BG) of supplementary information. The dye color starting
391 disappearing right after 30 minutes of irradiation and complete degradation was observed around 60
392 minutes of irradiation using novel Mn-BMG whereas, the decrease in the intensity was gradual with
393 time using ternary BMG and binary BG. The rapid decrease in intensity upon light irradiation is
394 signifying that chromophore groups responsible for imparting colour are breaking down slowly.
395 Further, the kinetic models are applied to this data.

396

397 **4.5 Kinetics of Photodegradation reaction.**

398 Two kinetic models first-order and second-order were studied for the photodegradation of dye
399 methylene blue by the doped and undoped ternary nanocomposites. The expression for each model is
400 expressed in equations 3-4

401

402 First-order kinetics:

$$403 \quad \ln \frac{C_0}{C_t} = k_1 t \quad \text{Eq..... (3)}$$

404

405

406 Second-order kinetics:

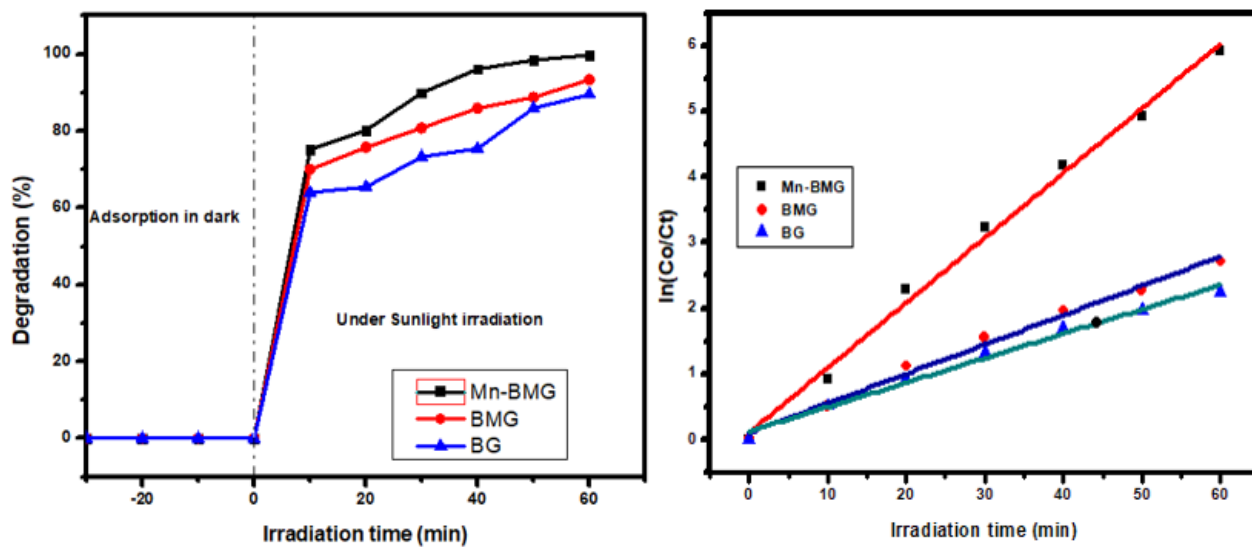
$$407 \quad \frac{1}{C_t} - \frac{1}{C_0} = k_2 t \quad \text{Eq..... (4)}$$

408

409

410 Fig. 8(b), shows a linear relationship between $\ln(C_0/C)$ and reaction time, where C_0 and C are the initial
411 concentrations, indicating that the photodegradation of methylene blue by doped and undoped ternary
412 nanocomposites follows first-order kinetics. The plot of C_0/C versus time represents a straight line
413 where the slope of which upon linear regression equals the apparent first-order rate constant k . The
414 higher rate constants k of Mn-BMG for the first-order reaction than undoped ternary indicates that Mn-
415 doped BWO-GO is more effective under sunlight than BWO-GO/MoS₂. The values of R^2 for the first-
416 order reaction for doped and undoped ternary composites are 0.9967 and 0.993 respectively, suggesting
417 that the ternary hybrids effectively follow the first order reaction. The rate constant k of the doped
418 component is more than that of undoped ternary revealing that doping has caused an acceleration in the
419 degradation rate under visible light A. The higher rate constant of doped BMG than other photocatalysts
420 explains that the Mn-BMG shows more photoefficiency than others. Comparison of correlation
421 coefficients for a first order and second order are shown in table 1.

422



423

424 **Fig.8** MB % removal as a function of time (a) photocatalytic degradation of MB in the presence of

425 sunlight, catalysts under optimum conditions (a) First order kinetic model fitting

426

427 **Table.1** Correlation coefficients (R^2) and kinetic parameters for MB ($C_0=10\text{ppm}$) degradation

Photocatalysts	Experimental conditions			First-order kinetics		Second-order kinetics	
	pH	Photocatalyst dose(mg/L)	Initial dye concentration(ppm)	$k_1(\text{min}^{-1})$	R^2	$K_2 (\text{L}\mu\text{mol}^{-1}\text{min}^{-1})$	R^2
Mn-BMG	8	50mg	10ppm	0.0866	0.9967	0.43215	0.729
BMG	8	50mg	10ppm	0.02899	0.993	0.14207	0.8616
BW	7	40mg	10ppm	0.0255	0.987	0.0886	0.8487

428

429 **4.6 Type of the Photocatalyst and the role of dopant species:**

430 The type of photocatalyst used is the most imperative parameter for greater photocatalytic degradation.

431 The bandgap, crystallinity, porosity, surface area and nature of dopant all determine the effectiveness

432 of catalyst in the visible light region. The ternary nanocomposites as compared to binary composites

433 show increased degradation due to the synchronized activation of the charge transfer mechanism

434 between the various semiconductor materials. The transfer of charges between the conduction bands of

435 two metal oxides leads and a support material leads to enhanced charge separation and less

436 agglomeration by increasing the specific surface area ultimately offering more active sites. The ternary

437 undoped BMG showed 94% degradation in visible light as compared to the binary counterpart.

438 The addition of dopant species in the semiconductor ternary system further improved the photocatalytic

439 activity which is mainly ascribed to alteration in the bandgap energy, following the transfer of energy.

440 The addition of dopant creates additional energy levels and leading to better separation and transfer of
441 photogenerated charge carriers to the surface of the catalyst. This separation mainly depends upon two
442 factors including large surface area and the light absorbed by the catalyst (Aydoghmesh et al. 2019). .
443 Therefore, the doped ternary Mn-BMG showed strong visible light region absorption and greater
444 degradation for methylene blue up to 99.7% in one hour.

445 **4.7 Degradation under UV irradiation**

446 A sole experiment was done in UV radiations considering the optimized conditions specific for all the
447 photocatalyst. Methylene blue was degraded almost completely in UV irradiation only after exposure
448 of half an hour by Mn-BMG. Undoped BMG and binary BG also performed well under ultraviolet light
449 and their ternary heterojunction has shown more than 90% degradation under UV light. Similar results
450 of greater MB degradation by ternary nanocomposite were shown earlier in UV light degradation
451 (Aydoghmesh et al., 2019).

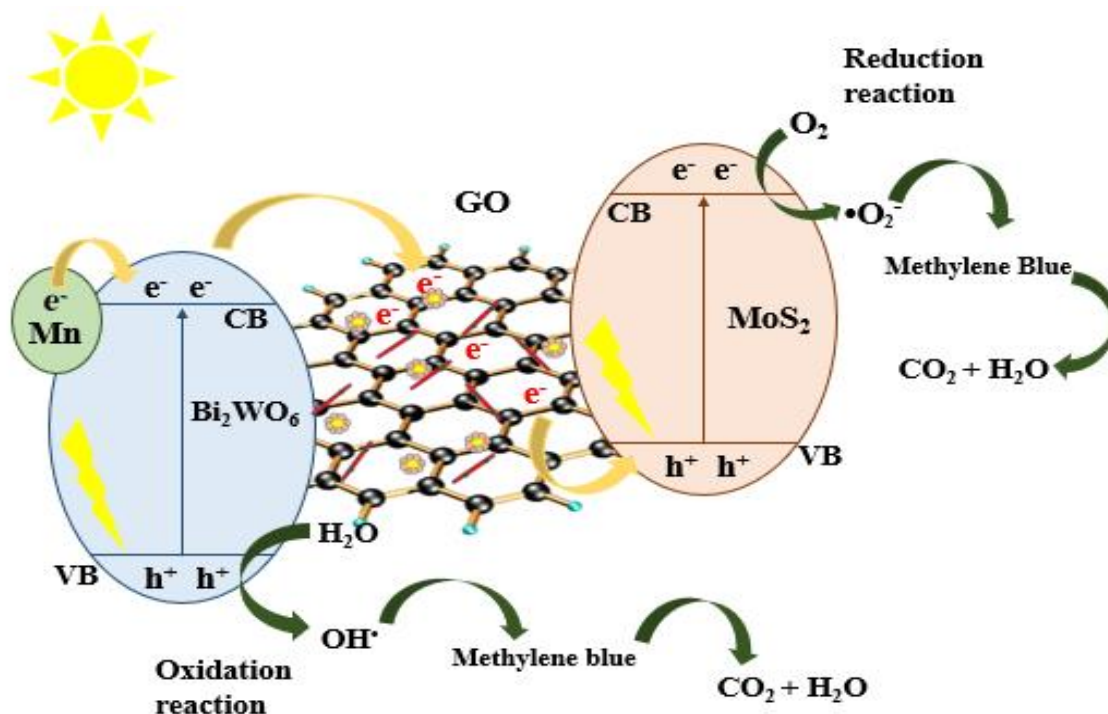
452

453 **5. Radical Scavenging and proposed mechanism**

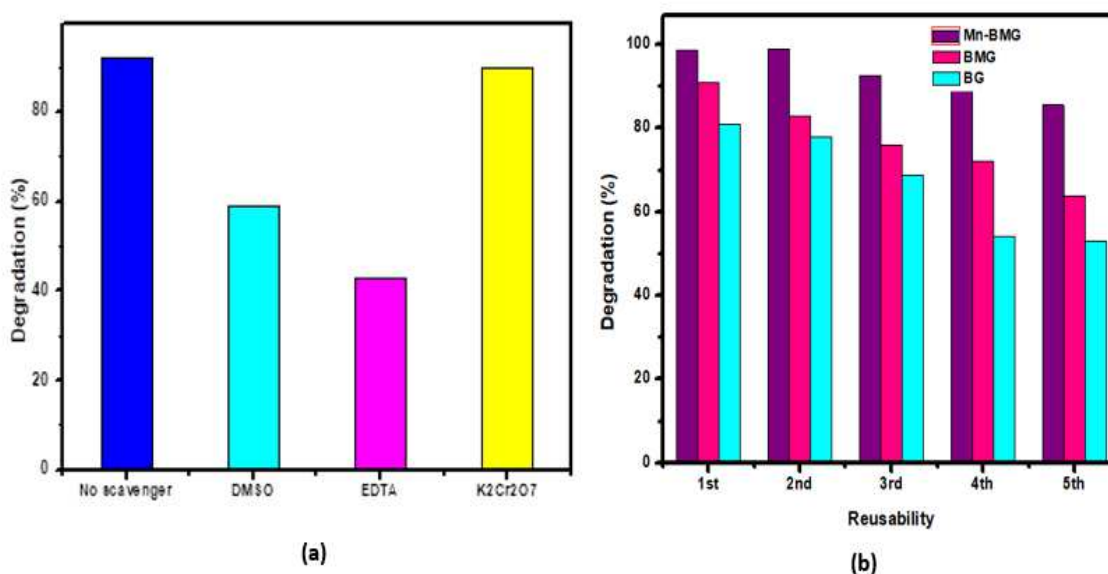
454 The determination of active species involved in the photocatalytic process is significant for
455 understanding the degradation mechanism of organic pollutants. In the degradation of dyes, several
456 active radical species such as hydroxyl radicals ($\text{OH}\cdot$), holes, (h^+), electron (e^-) superoxide anion
457 radical ($\cdot\text{O}^{2-}$) play a vital role (Rajendran et al., 2018). Hence, to investigate the key active species
458 involved during the photocatalytic process, a radical scavenging experiment was performed. 5mM of
459 EDTA (ethylene-diamine-tetra-acetate), $\text{K}_2\text{Cr}_2\text{O}_7$ (potassium dichromate), DMSO (dimethyl sulfoxide)
460 were used to scavenge holes, electrons and hydroxyl radicals. The experiment was performed under
461 sunlight. From fig.10(b) it is clear that EDTA is the main radical scavenger in the degradation process
462 of MB by MnBW-GO/MoS₂, as the addition of EDTA decreased the degradation values from 99 to
463 48.83. The addition of DMSO decreased the degradation from 99 to 55% indicating that hydroxyl
464 radicals also have a contributing role in addition to holes. Very little change was observed by the
465 addition of $\text{K}_2\text{Cr}_2\text{O}_7$ indicating that electrons do not play a major role in MB degradation by Mn-BWO-
466 GO/MoS₂.

467 The proposed mechanism of MB degradation by Mn-BWO-GO/MoS₂, suggests that holes and hydroxyl
468 radicals are the main active species. Holes are directly responsible for degradation and producing more
469 hydroxyl radicals. Upon sunlight irradiation, both Bi_2WO_6 and MoS₂ are excited and produce electrons
470 and holes. The photoexcited electrons get transferred from the conduction band of MoS₂ having a
471 negative potential towards the conduction band of Bi_2WO_6 having a positive potential. While the
472 photoinduced holes accumulate above the Valence band of MoS₂. The reactive holes accumulated on
473 the surface of MoS₂ directly oxidize MB dye molecules adsorbed on the catalyst surface. Graphene
474 oxide has a large surface area and electrical conductivity acts as a mediator and transfers electrons to
475 and from MoS₂ and Bi_2WO_6 . Mn doping introduces additional energy levels in BWO, hence photo-
476 induced electrons and holes take longer to recombine. Eventually, the photo-response of the ternary

477 heterojunction is increased towards visible light. A similar mechanism has been proposed by Lv et al.,
 478 (Lv et al., 2017). Hence, holes are responsible for the degradation of dyes and production of hydroxyl
 479 radicals whereas, the influence of electrons and superoxide anions is relatively less. Fig 9 shows the
 480 degradation mechanism by ternary Mn-BWO-GO/MoS₂.



481
 482
 483 **Fig.9** Photocatalytic degradation mechanism of Dye Methylene blue by Mn-BWO-GO/MoS₂



484
 485 **Fig. 10** (a) Study of various radical scavengers (b) reusability of Mn-BMG, BMG, BW nanocomposites
 486 **6. Reusability:**

487 Under the optimized conditions for each photocatalyst, the stability of catalysts was confirmed by using
488 the catalysts repeatedly in five successive trials. For this, the catalysts are separated from the treated
489 MB dye solution by centrifugation then rinsed thrice using distilled water and later dried up at 60°C in
490 an electric oven. The catalysts are then weighed and investigated for their photocatalytic efficiency. All
491 the reusability trials are run at the same optimized conditions for each catalyst i.e at pH 8, catalyst dose-
492 50mg/100m, IDC 10ppm for doped undoped ternary nanocomposite, and pH 7, catalyst dose
493 40mg/100ml, IDC 10ppm for binary BW-GO. No substantial loss in photocatalytic activity was
494 observed after five runs with just a 10% decrease in catalytic activity fig.10(b). The results revealed
495 that the ternary doped composite exhibits high mechanical stability and reuseability.

496 **Conclusion:**

497 The novel ternary hybrid Mn-BWO-GO/MoS₂ has found valuable applications for Organic pollutants
498 degradation. The doped ternary photocatalyst was synthesized by an insitu hydrothermal method. The
499 ternary hybrid showed excellent degradation for dye Methylene blue under sunlight irradiation.
500 Undoped ternary BW-GO/MoS₂, and binary BW-GO were also prepared to compare the degradation
501 efficiencies of doped and undoped ternary hybrids with binary composite. The Mn-BWO-GO/MoS₂
502 showed 99% MB degradation in an hour. The improved photocatalytic efficiency was credited to the
503 ternary heterojunction formed as a result of BWO, MoS₂, and GO. The ternary heterojunction has the
504 characteristics of all three components and the Mn doping further suppresses the electron-holes
505 recombination. The photostability of photocatalysts was evaluated by five consecutive runs with less
506 than 10% reduction in degradation.

507 **Declarations:**

508 *Ethical Approval and Consent to Participate* Not applicable

509 *Consent to Publish* All the author agree to publish this article

510 *Authors Contributions*

511 **Noor Tahir:** Data curation, Visualization, Investigation, Writing - original draft, Writing -
512 review & editing. **Muhammad Zahid:** Conceptualization, Project administration, Resources,
513 Supervision, Writing - review & editing. **Ijaz Ahmad Bhatti:** Conceptualization,
514 Methodology, Software, Writing - review & editing. **Yasir Jamil:** Visualization, Investigation,
515 Validation.

516 *Funding*

517 This research was funded by the Higher Education Commission (HEC), Pakistan, under Indigenous
518 5000 PhD Fellowship with student pin number “pin # 518-121977-2PS5-032 (50043428)”.

519 *Competing Interests*

520 The authors have no conflicts of interest to declare that are relevant to the content of this article.

521 **Availability of data and materials**

522 The datasets used and/or analyzed in this study are available in the manuscript and supplementary
523 information additional information can be asked from the corresponding author upon request.

524

525

526

527 **References:**

- 528 Ahmad I (2019) Inexpensive and quick photocatalytic activity of rare earth (Er, Yb) co-doped ZnO
529 nanoparticles for degradation of methyl orange dye. *Separation and Purification Technology*
530 227: 115-126
- 531 Ahmad M, Khan MY, Sadaf S, Iqbal S, Nawaz F, Iqbal J (2019) Novel indigo-dye-doped graphene-
532 supported Mn/WO₃ nanocomposite as visible light photocatalyst for degradation of
533 methylene blue dye. *Materials Research Express* 6(5): 055050
- 534 Ahmadi S, Rahdar A, Igwegbe CA, Mortazavi-Derazkola S, Banach AM, Rahdar S, Singh AK, Rodriguez-
535 Couto S, Kyzas GZ (2020) Praseodymium-doped cadmium tungstate (CdWO₄) nanoparticles
536 for dye degradation with sonocatalytic process. *Polyhedron* 190: 114792
- 537 Aydoghmish SM, Hassanzadeh-Tabrizi S, Saffar-Teluri A (2019) Facile synthesis and investigation of
538 NiO–ZnO–Ag nanocomposites as efficient photocatalysts for degradation of methylene blue
539 dye. *Ceramics International* 45(12): 14934-14942
- 540 Aziz A, Ali N, Khan A, Bilal M, Malik S, Ali N, Khan H (2020) Chitosan-zinc sulfide nanoparticles,
541 characterization and their photocatalytic degradation efficiency for azo dyes. *International*
542 *Journal of Biological Macromolecules* 153: 502-512
- 543 Chanu LA, Singh WJ, Singh KJ, Devi KN (2019) Effect of operational parameters on the photocatalytic
544 degradation of Methylene blue dye solution using manganese doped ZnO nanoparticles.
545 *Results in Physics* 12: 1230-1237
- 546 Dou R, Cheng H, Ma J, Komarneni S (2020) Manganese doped magnetic cobalt ferrite nanoparticles
547 for dye degradation via a novel heterogeneous chemical catalysis. *Materials Chemistry and*
548 *Physics* 240: 122-181
- 549 Hou X, Wang Z, Fan G, Ji H, Yi S, Li T, Wang Y, Zhang Z, Yuan L, Zhang R (2020) Hierarchical three-
550 dimensional MoS₂/GO hybrid nanostructures for triethylamine-sensing applications with high
551 sensitivity and selectivity. *Sensors and Actuators B: Chemical* 317: 128-236
- 552 Hu K, Chen C, Zhu Y, Zeng G, Huang B, Chen W, Liu S, Lei C, Li B, Yang Y (2019) Ternary Z-scheme
553 heterojunction of Bi₂WO₆ with reduced graphene oxide (rGO) and meso-tetra (4-
554 carboxyphenyl) porphyrin (TCPP) for enhanced visible-light photocatalysis. *Journal of colloid*
555 *and interface science* 540: 115-125
- 556 Huang F, Yan A, Zhao H. (2016). Influences of doping on photocatalytic properties of TiO₂
557 photocatalyst. In C. Wenbin (Ed.), *Semiconductor photocatalysis-materials, mechanisms and*
558 *applications*, IntechOpen, London pp. 31-80
- 559 Khojeh B, Zanjanchi M, Golmojdeh H (2017) Preparation of catalytically active bismuth tungstate:
560 effects of organic additives and dopants. *Materials Research Innovations* 21(5): 341-349
- 561 Li B, Lai C, Zeng G, Qin L, Yi H, Huang D, Zhou C, Liu X, Cheng M, Xu P (2018) Facile hydrothermal
562 synthesis of Z-scheme Bi₂Fe₄O₉/Bi₂WO₆ heterojunction photocatalyst with enhanced visible
563 light photocatalytic activity. *ACS applied materials & interfaces* 10(22): 18824-18836
- 564 Li F, Zhang L, Li J, Lin X, Li X, Fang Y, Huang J, Li W, Tian M, Jin J (2015) Synthesis of Cu–MoS₂/rGO
565 hybrid as non-noble metal electrocatalysts for the hydrogen evolution reaction. *Journal of*
566 *Power Sources* 292: 15-22
- 567 Liu M, Xue X, Yu S, Wang X, Hu X, Tian H, Chen H, Zheng W (2017) Improving photocatalytic
568 performance from Bi₂WO₆@ MoS₂/graphene hybrids via gradual charge transferred pathway.
569 *Scientific reports* 7(1): 1-11
- 570 Lv H, Liu Y, Tang H, Zhang P, Wang J (2017) Synergetic effect of MoS₂ and graphene as cocatalysts for
571 enhanced photocatalytic activity of BiPO₄ nanoparticles. *Applied Surface Science* 425: 100-106
- 572 Mafa PJ, Ntsendwana B, Mamba BB, Kuvarega AT (2019) Visible light driven ZnMoO₄/BiFeWO₆/rGO Z-
573 scheme photocatalyst for the degradation of anthraquinonic dye. *The Journal of Physical*
574 *Chemistry C* 123(33): 20605-20616
- 575 Mudhoo A, Paliya S, Goswami P, Singh M, Lofrano G, Carotenuto M, Carraturo F, Libralato G, Guida M,
576 Usman M (2020) Fabrication, functionalization and performance of doped photocatalysts for
577 dye degradation and mineralization: a review. *Environmental Chemistry Letters* 18: 1825-1903

578 Mushtaq F, Zahid M, Mansha A, Bhatti I, Mustafa G, Nasir S, Yaseen M (2020) MnFe₂O₄/coal fly ash
579 nanocomposite: a novel sunlight-active magnetic photocatalyst for dye degradation.
580 International Journal Of Environmental Science And Technology 17(10): 4233-4248
581 Nawaz A, Khan A, Ali N, Ali N, Bilal M (2020) Fabrication and characterization of new ternary ferrites-
582 chitosan nanocomposite for solar-light driven photocatalytic degradation of a model textile
583 dye. Environmental Technology & Innovation 20: 79-100
584 Nguyen DCT, Cho KY, Jung C-H, Oh W-C (2018) Photocatalytic activities of contaminants by Bi₂WO₆-
585 graphene composites decorated with mesoporous silica. Journal of Alloys and Compounds
586 766: 477-487
587 Nie M, Yang Y, Zhang Z, Yan C, Wang X, Li H, Dong W (2014) Degradation of chloramphenicol by
588 thermally activated persulfate in aqueous solution. Chemical Engineering Journal 246: 373-
589 382
590 Rajendran R, Varadharajan K, Jayaraman V, Singaram B, Jeyaram J (2018) Photocatalytic degradation
591 of metronidazole and methylene blue by PVA-assisted Bi₂WO₆-CdS nanocomposite film under
592 visible light irradiation. Applied Nanoscience 8(1): 61-78
593 Reddy CV, Reddy IN, Akkinapally B, Harish V, Reddy KR, Jaesool S (2019) Mn-doped ZrO₂ nanoparticles
594 prepared by a template-free method for electrochemical energy storage and abatement of
595 dye degradation. Ceramics International 45(12): 15298-15306
596 Saher R, Hanif M, Mansha A, Javed H, Zahid M, Nadeem N, Mustafa G, Shaheen A, Riaz O (2021)
597 Sunlight-driven photocatalytic degradation of rhodamine B dye by Ag/FeWO₄/gC₃N₄
598 composites. International Journal Of Environmental Science And Technology 18(4): 927-938
599 Senthil RA, Osman S, Pan J, Sun Y, Kumar TR, Manikandan A (2019) A facile hydrothermal synthesis of
600 visible-light responsive BiFeWO₆/MoS₂ composite as superior photocatalyst for degradation
601 of organic pollutants. Ceramics International 45(15): 18683-18690
602 Singh P, Shandilya P, Raizada P, Sudhaik A, Rahmani-Sani A, Hosseini-Bandegharai A (2020) Review
603 on various strategies for enhancing photocatalytic activity of graphene based nanocomposites
604 for water purification. Arabian Journal of Chemistry 13(1): 3498-3520
605 Tabasum A, Alghuthaymi M, Qazi UY, Shahid I, Abbas Q, Javaid R, Nadeem N, Zahid M (2021) UV-
606 Accelerated Photocatalytic Degradation of Pesticide over Magnetite and Cobalt Ferrite
607 Decorated Graphene Oxide Composite. Plants 10(1): 1-6
608 Tabasum A, Bhatti IA, Nadeem N, Zahid M, Rehan ZA, Hussain T, Jilani A (2020) Degradation of
609 acetamiprid using graphene-oxide-based metal (Mn and Ni) ferrites as Fenton-like
610 photocatalysts. Water Sci Technol 81(1): 178-189
611 Tabasum A, Zahid M, Bhatti HN, Asghar M (2019) Fe₃O₄-GO composite as efficient heterogeneous
612 photo-Fenton's catalyst to degrade pesticides. Materials Research Express 6(1): 015608
613 Wang J, Tang L, Zeng G, Liu Y, Zhou Y, Deng Y, Wang J, Peng B (2017) Plasmonic Bi metal deposition
614 and g-C₃N₄ coating on Bi₂WO₆ microspheres for efficient visible-light photocatalysis. ACS
615 Sustainable Chemistry & Engineering 5(1): 1062-1072
616 Yang J, Wang X, Zhao X, Dai J, Mo S (2015) Synthesis of uniform Bi₂WO₆-reduced graphene oxide
617 nanocomposites with significantly enhanced photocatalytic reduction activity. The Journal of
618 Physical Chemistry C 119(6): 3068-3078
619 Zhou H, Liu Y, Zhang L, Li H, Liu H, Li W (2019) Transition metal-doped amorphous molybdenum
620 sulfide/graphene ternary cocatalysts for excellent photocatalytic hydrogen evolution:
621 Synergistic effect of transition metal and graphene. Journal of colloid and interface science
622 533: 287-296
623 Zolgharnein J, Rastgordani M (2018) Multivariate optimization and characterization of simultaneous
624 removal of binary mixture of Cu (II) and Pb (II) using Fe₃O₄@MoS₂ nanoparticles. Journal of
625 Chemometrics 32(9): 30-43
626
627

Figures

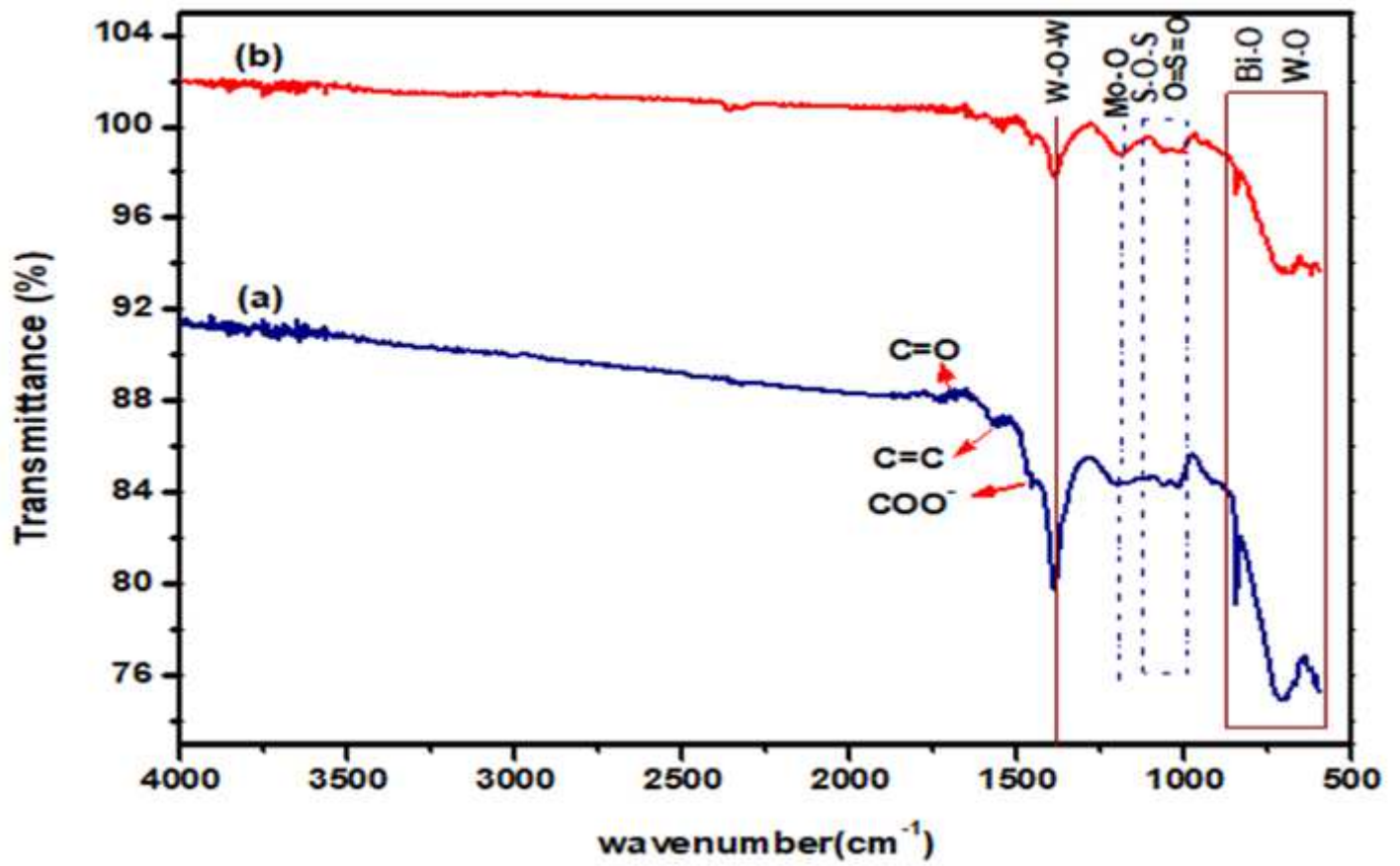


Figure 1

FTIR spectra of (a) BMG and (b) Mn-BMG ternary nanocomposites

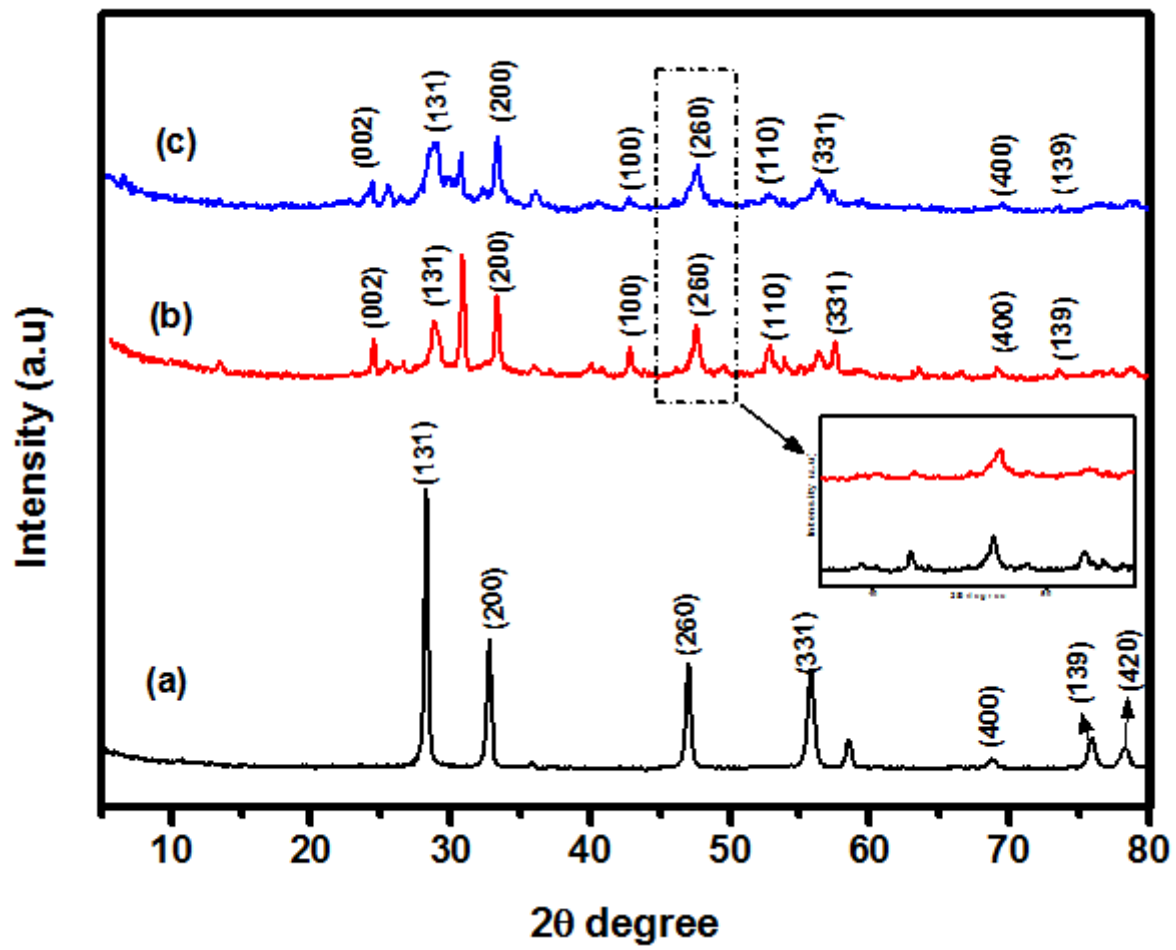


Figure 2

X-ray diffraction patterns of (a) BG (b) BMG and (c) Mn-BMG nanocomposites

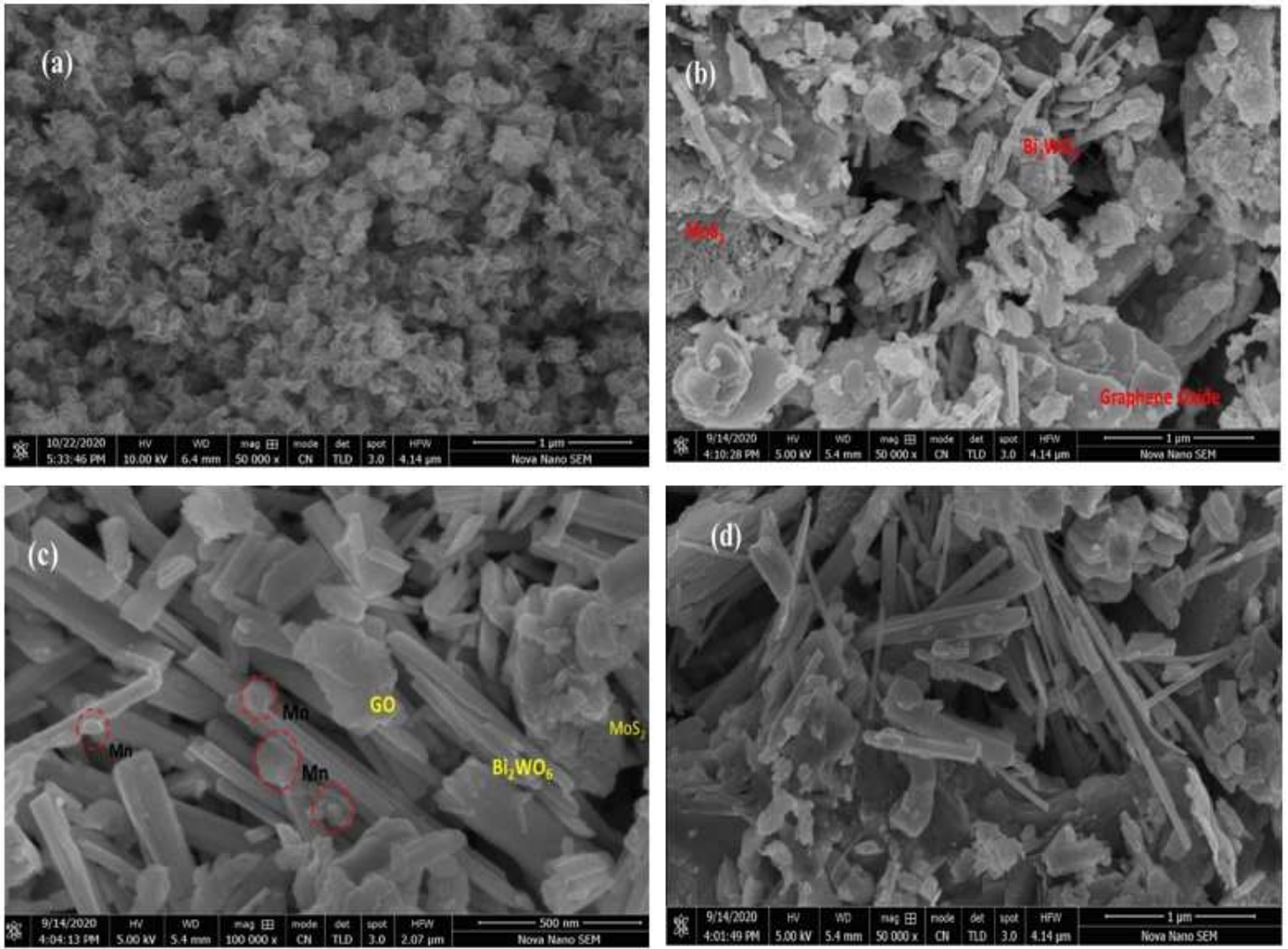


Figure 3

SEM images of (a) MoS₂ nanoflowers (b) BMG (c & d) Mn-BMG

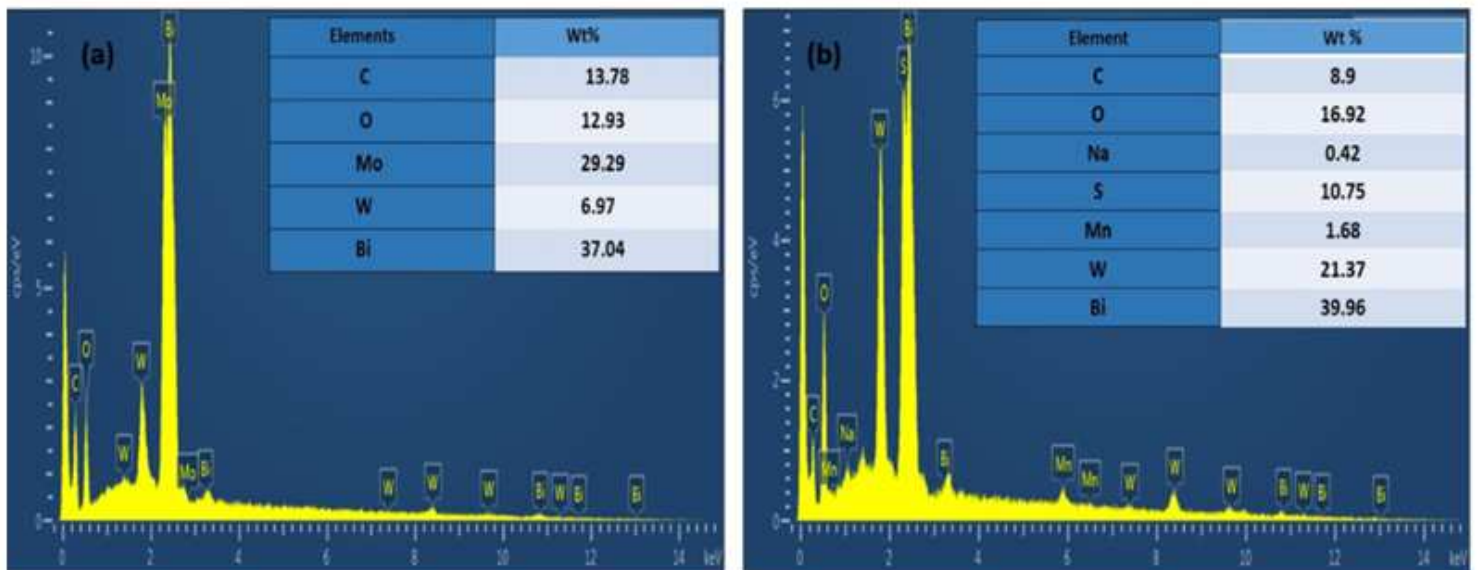


Figure 4

EDX spectra of (a)BMG (b) Mn- BMG ternary nanocomposites

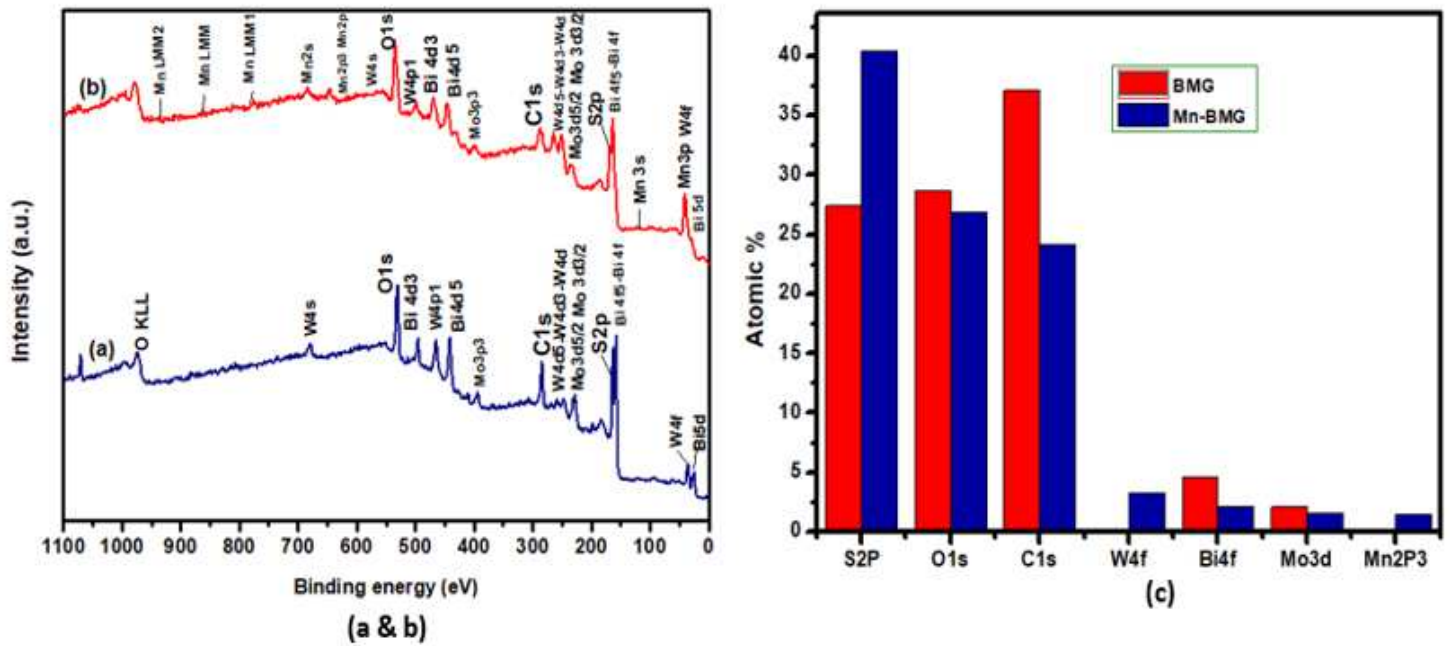


Figure 5

XPS survey spectrum of (a) BMG (b) Mn-BMG and (c) atomic percentages of BMG and Mn-BMG

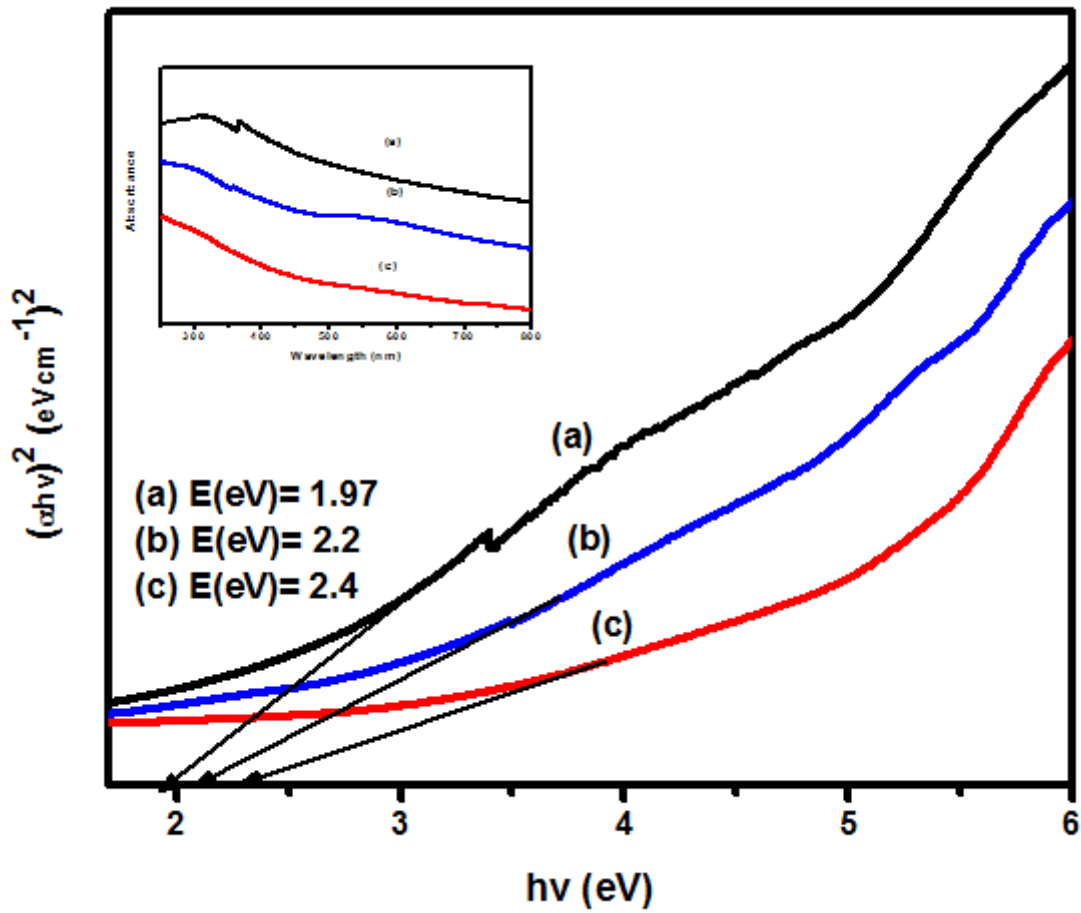


Figure 6

Bandgap energies estimation of (a) BG and (b) Mn-BMG (c) BMG by Tauc plot method with inset showing the UV-VIS absorption spectra of the BMG and Mn-BMG

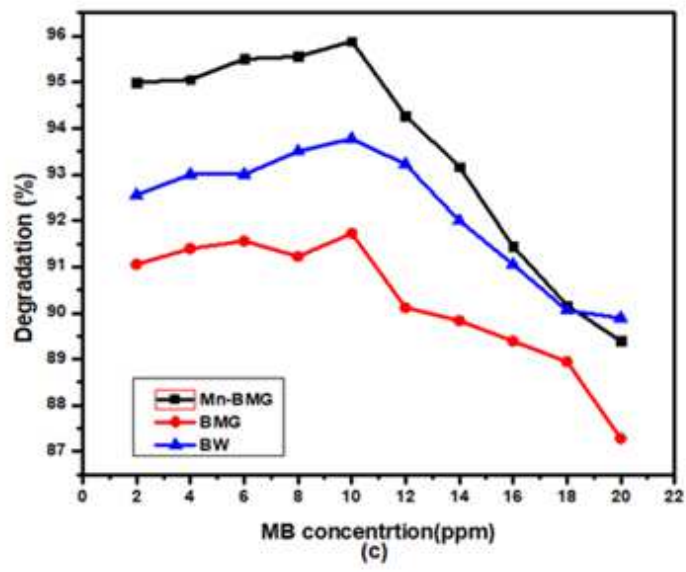
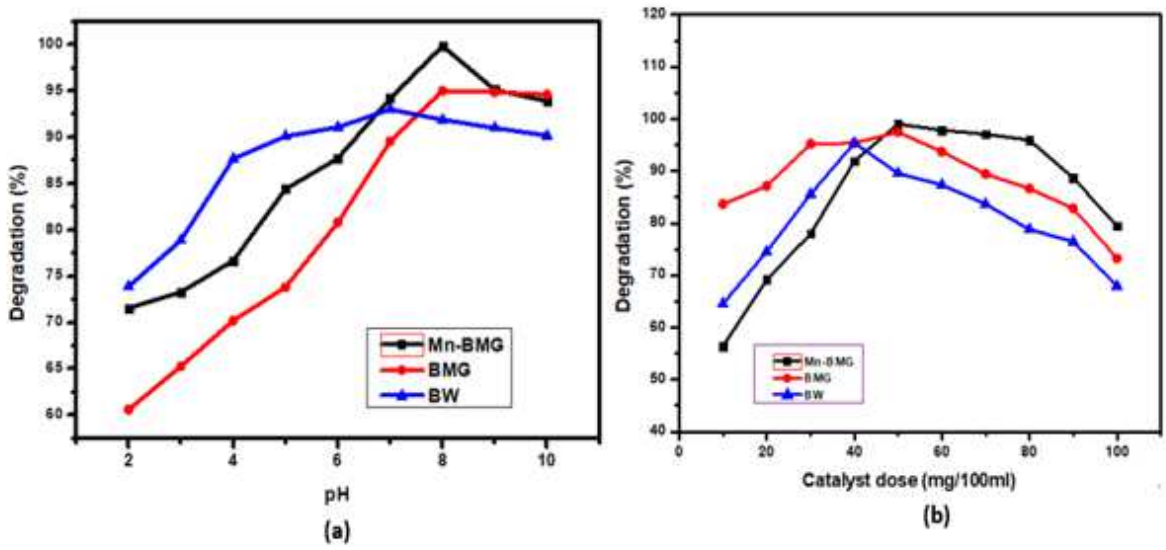


Figure 7

Optimization of reaction parameters using Mn-BMG, BMG and BW (a) pH, (b) catalyst dose, (c) Initial dye concentration

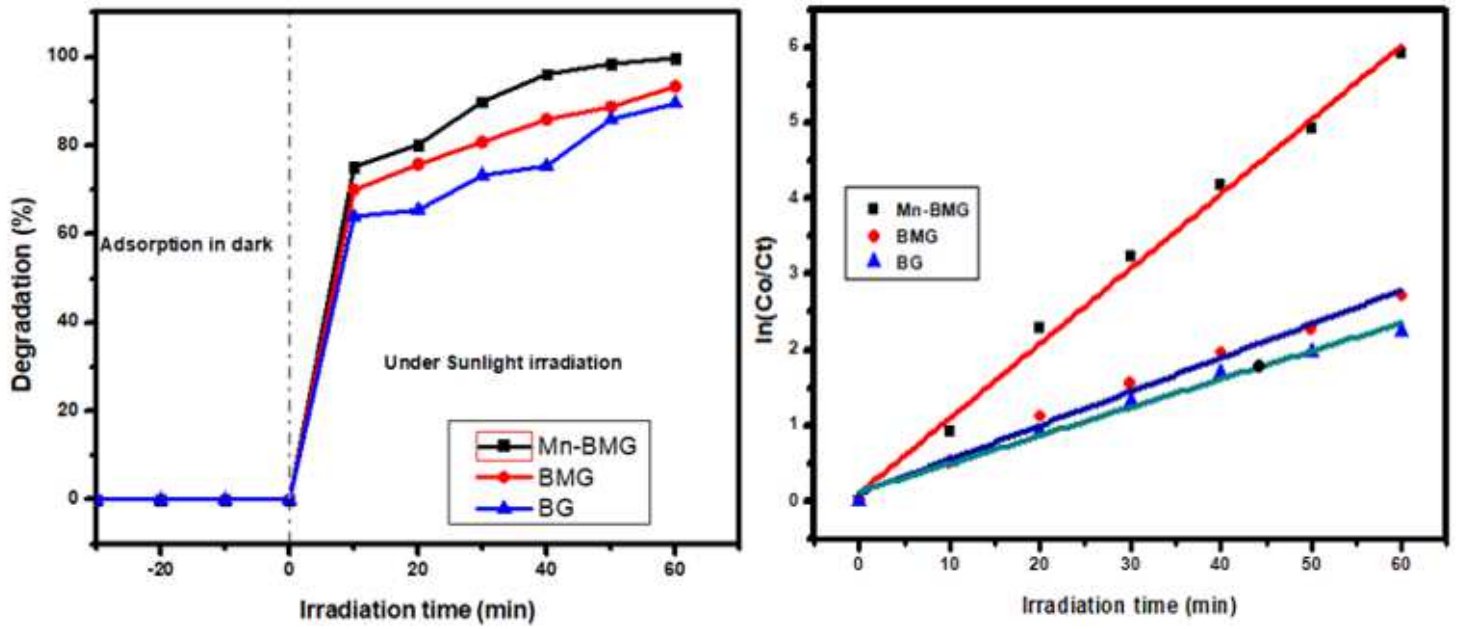


Figure 8

MB % removal as a function of time (a) photocatalytic degradation of MB in the presence of sunlight, catalysts under optimum conditions (a) First order kinetic model fitting

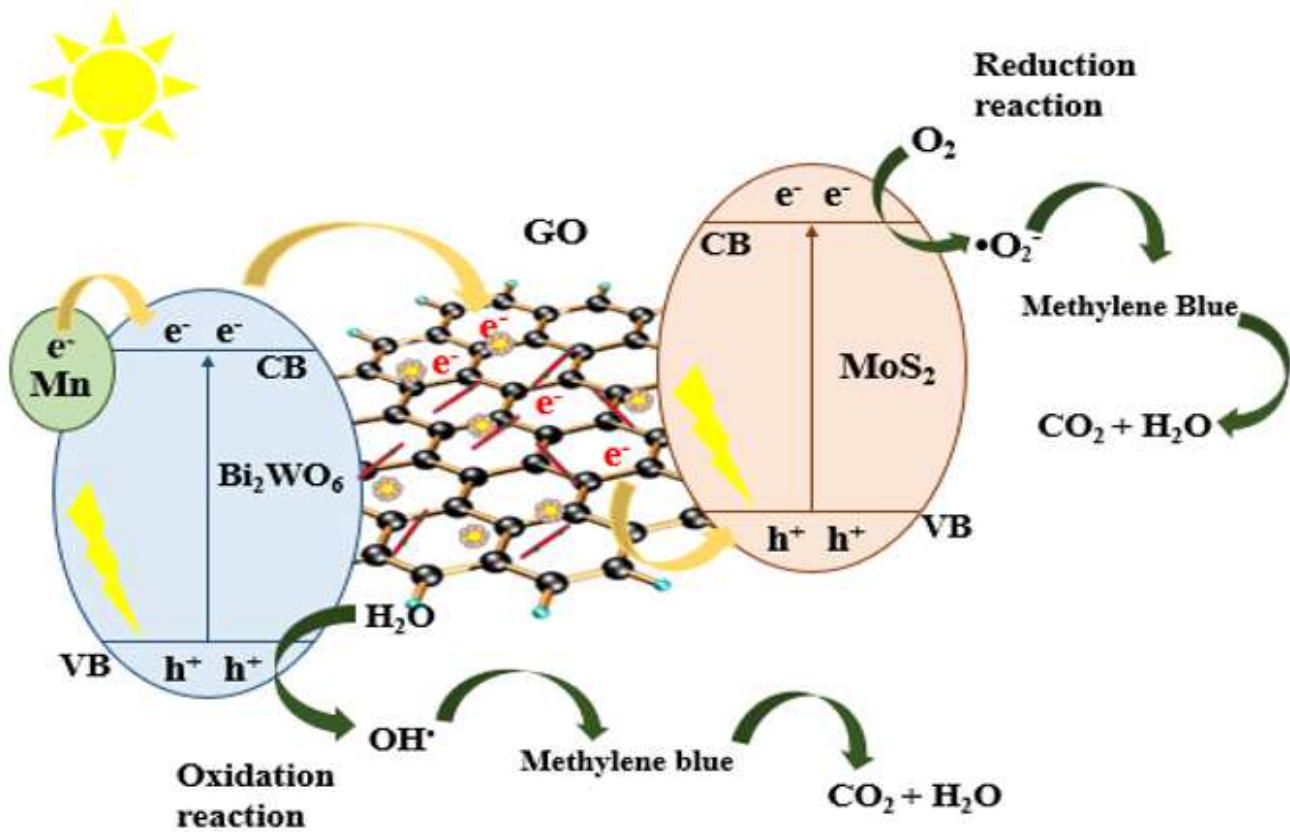


Figure 9

Photocatalytic degradation mechanism of Dye Methylene blue by Mn-BWO-GO/MoS₂

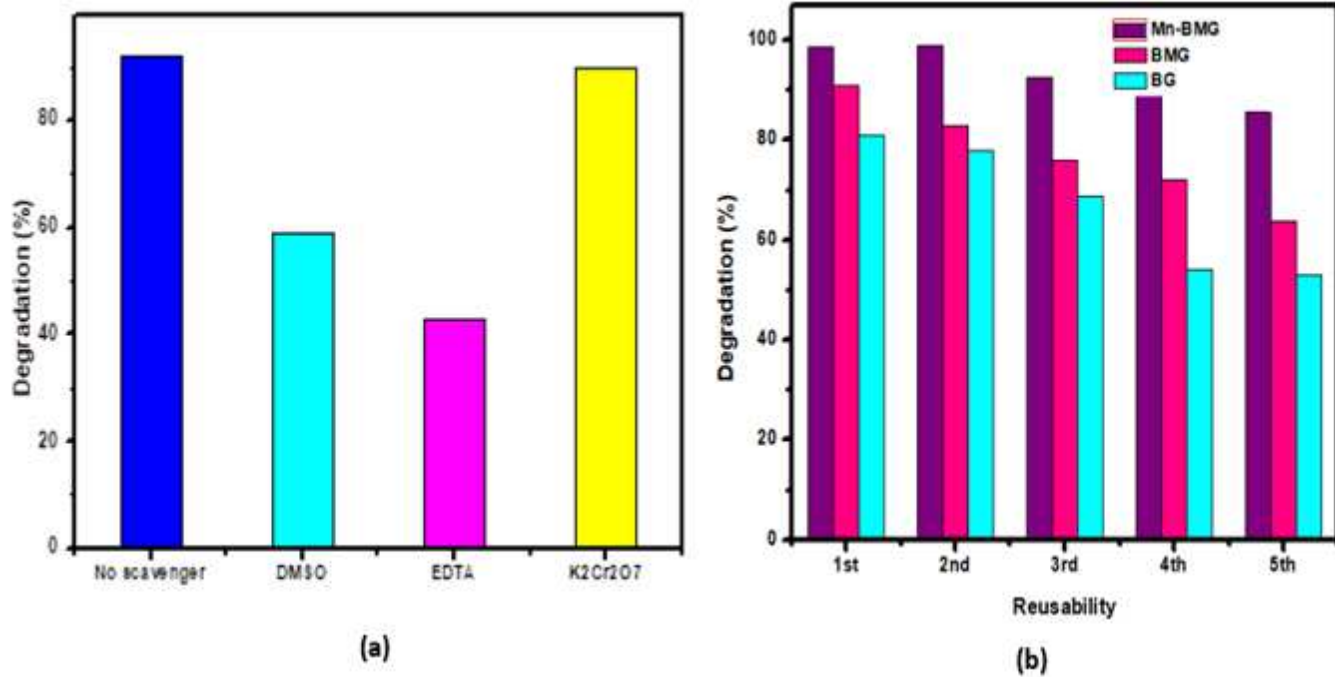


Figure 10

(a) Study of various radical scavengers (b) reusability of Mn-BMG, BMG, BW nanocomposites

Supplementary Files

This is a list of supplementary files associated with this preprint. Click to download.

- [SUPPLEMENTARYINFORMATION.docx](#)